NASA-TM-111592

AIAA 96-1735
Aeroacoustic Codes For Rotor Harmonic and BVI Noise—CAMRAD.Mod1/HIRES

Thomas F. Brooks
NASA Langley Research Center
Hampton, VA

D. Douglas Boyd, Jr.
Lockheed Engineering and Sciences Co.
Hampton, VA

Casey L. Burley
NASA Langley Research Center
Hampton, VA

J. Ralph Jolly, Jr.
4 Office Park Circle
Birmingham, AL

2nd AIAA/CEAS Aeroacoustics Conference
May 6-8, 1996 / State College, PA

AEROACOUSTIC CODES FOR ROTOR HARMONIC AND BVI NOISE—CAMRAD.Mod1/HIRES

*Thomas F. Brooks**
NASA Langley Research Center, Hampton, VA

D. Douglas Boyd, Jr.†
Lockheed Engineering and Sciences Company, Hampton, VA

Casey L. Burley‡
NASA Langley Research Center, Hampton, VA

J. Ralph Jolly, Jr.§
4 Office Park Circle, Birmingham, AL

Abstract

This paper presents a status of non-CFD aeroacoustic codes at NASA Langley Research Center for the prediction of helicopter harmonic and Blade-Vortex Interaction (BVI) noise. The prediction approach incorporates three primary components: CAMRAD.Mod1 - a substantially modified version of the performance/trim/wake code CAMRAD; HIRES - a high resolution blade loads post-processor; and WOPWOP - an acoustic code. The functional capabilities and physical modeling in CAMRAD.Mod1/HIRES will be summarized and illustrated. A new multi-core roll-up wake modeling approach is introduced and validated. Predictions of rotor wake and radiated noise are compared with to the results of the HART program, a model BO-105 windtunnel test at the DNW in Europe. Additional comparisons are made to results from a DNW test of a contemporary design four-bladed rotor, as well as from a Langley test of a single proprotor (tiltrotor) three-bladed model configuration. Because the method is shown to help eliminate the necessity of guesswork in setting code parameters between different rotor configurations, it should prove useful as a rotor noise design tool.

Symbols

A	most inboard y value associated with the tip vortex, m
B	most inboard y value associated with the secondary vortex, m
C	y value about which the secondary vortex forms, m
C_T	rotor thrust coefficient, thrust/$\rho\pi R^2(\Omega R)^2$
c	blade chordlength, m
R	rotor radius, m
r	radial distance along blade, m
r	distance from vortex center, m
r_c	effective vortex viscous core radius, m
r_v	measured vortex viscous core radius, m
r', r''	radial distances from C, see Equation (11), m
X	streamwise coordinate relative to hub, positive downstream, m
Y	cross-flow coordinate relative to hub, positive on advancing side, m
y	radial distance, as measured radially from the tip, m
$\bar{y}$	centroid of vortex, as measured radially from the tip, m
Z	vertical coordinate relative to hub, in line with rotor shaft axis, m
v	swirl velocity associated with vortex, m/s
α_s	rotor shaft angle referenced to tunnel streamwise axis, positive for backward tilt, deg
δl	increment change in vortex line filament length, see Figure 10, m
Γ	vortex circulation, m^2/s
Γ'	change in circulation from one radius or station to another, m^2/s
μ	advance ratio, tunnel flow velocity/ΩR
ρ	air density, kg/m^3
Ω	rotor rotational speed, rad/s or rpm
Ψ	blade azimuth angle, deg

*Senior Research Scientist, FMAD, Associate Fellow AIAA
†Engineer
‡Research Scientist, Member AIAA
§Engineer

subscripts

n	integer
p	vortex element number, integer
P	total number of radial elements in multi-core vortex model
s	secondary vortex
t	tip vortex
+ max	value of function at maximum positive Γ
− max	value of function at maximum negative Γ

Introduction

Early forms of the non-CFD aeroacoustic rotor codes were developed at Langley in support of Higher Harmonic Control (HHC) / Blade Vortex Interaction (BVI) noise reduction studies[1]. Since then, the codes have been under development and application. The codes have evolved to become key elements of a system noise prediction capability called TRAC, for Tilt Rotor Aeroacoustic Codes, being developed under the Short Haul (Civil Tiltrotor) or SH(CT) Program between NASA and the US helicopter industry. The purpose of TRAC is to provide analysis for the design and evaluation of efficient low-noise tiltrotor blades, as well as to support the development of safe, low-noise flight approaches. TRAC is comprised of sets of interfaced CFD and non-CFD codes as illustrated in Figure 1. CAMRAD.Mod1 provides the performance/trim/wake information as input to the choice of alternate high resolution blade loads post-processors — one being a CFD approach by the use of FPRBVI[2], a Full Potential Rotor code that has been refined for impulsive BVI loading determination. The other is the HIRES code which is non-CFD and a subject of this paper. The high resolution blade loading from either method is employed in the acoustic code WOPWOP[3], which implements the acoustic formulation 1A of Farassat[4] to predict the acoustic pressure.

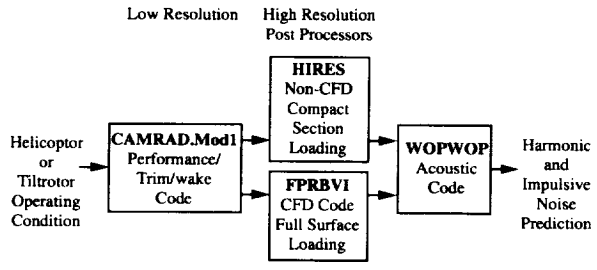

Figure 1: Key elements of the TiltRotor Aeroacoustic Codes (TRAC).

The use of FPRBVI provides chordwise distributions of the blade loading, whereas HIRES renders a chordwise compact loading. The choice of using one method of load determination over another would depend on the application. The FPRBVI approach may be preferred where flow over the blade is transonic or where substantial cross-flow (3D effects) occurs due to blade curvature. Such a CFD approach is also needed when alternate acoustic analysis to the code WOPWOP is used — such as Kirchhoff methods[5] or full-quadrupole methods[6,7] — which require velocity and pressure specification over a surface or a volume about the blade, respectively. However, the HIRES approach should be adequate for predicting noise for subsonic to low-transonic conditions where 2D sectional loading, and thus a lifting line analysis, is generally valid. In fact, the lifting line analysis is both a limitation as well as an advantage for HIRES; the advantage being that it can more readily account for full ranges of aerodynamic behavior such as unsteady separation and stall, than can current CFD approaches. A key advantage for HIRES has been its relative speed compared to FPRBVI. At Langley, HIRES has been the primary vehicle to validate the effect of new modeling within CAMRAD.Mod1 on blade loading and noise.

The present paper is intended to present key features of the CAMRAD.Mod1 and HIRES methods, as well as to partially validate the codes using experimental results from several rotor model noise tests, especially from the HART Program[8,9,10]. The HHC Aeroacoustic Rotor Test (HART), under the management of the U.S. Army Aeroflightdynamics Directorate (AFDD) at NASA Ames Research Center, was a cooperative test involving the DLR of Germany, ONERA of France, and both AFDD and NASA of the USA. The effort emphasized benchmark measurements and prediction of the wake, blade loads, and acoustics for both HHC and non-HHC rotor conditions. Prediction comparisons[11,12,13,14] with results from the test have demonstrated substantial progress in predicting harmonic and BVI noise, as well as pointing out necessary refinements that were needed in the codes — in particular, in the definition of the tip vortices within the wake. Since these early applications, new features, including modeling for the wake's tip vortex roll-up process, has been installed in the CAMRAD.Mod1/HIRES codes. Comparisons in this paper of predictions with data from several windtunnel model tests illustrate the degree of generality of the methodology.

Aeroacoustic Prediction Codes

The following describes details of the CAMRAD.Mod1/HIRES codes and WOPWOP of Figure 1 and their installed capabilities.

CAMRAD.Mod.1

The first step in the aeroacoustic calculations is perform a comprehensive performance/trim/wake analysis of the rotor. A highly modified version of the original rotor performance code CAMRAD[15], designated as CAMRAD.Mod1, has been developed at Langley for this purpose. CAMRAD.Mod1 (as well as HIRES) has been developed for use with rotors in windtunnels, conventional helicopter, and tiltrotors. A number of modifications and enhanced capabilities have been installed:

- CAMRAD was originally written by Wayne Johnson to use 15 degree azimuth steps in the free-wake geometry calculations, but was modified to 10 degree steps (a practical limit) by mostly redimensioning code arrays. The CAMRAD.Mod1 results are all resolved to 10 degree steps and referred to as the low resolution results in this paper.

- HHC and Individual Blade Control (IBC) of blade pitch can be input at the rotor hub. Allowance is made to include up to 12 harmonics (12P) of open-loop blade pitch control. This is accounted for in the aerodynamics and aeroelastic trim of the rotor.

- For blade motion, an option has been installed to employ either measured motion or calculated motion from external dynamic codes. This is done by by-passing the existing dynamic calculation and imposing on the trim solution a prescribed blade motion. It is required to cast the prescribed deflections in the form of harmonics of modal amplitudes. The elastic motion is separated in two parts — one being the flap/lag mode shapes and the other being the torsion modes. The collective and cyclic control angles are specified separately (these can also be determined in a trim analysis as discussed in an application to follow). The control angles combine with the elastic pitch from the torsion modes to give the total blade pitch at any radius. If measured or otherwise externally specified blade dynamics are not available, the unaltered rotor blade dynamics coding of CAMRAD may be used.

- Aerodynamic effects due to swept planforms is now be included. Existing coding for yawed flow effects was modified to include a swept planform in the corrections required for dynamic pressure and Mach Number. Planforms for which the elastic axis is not straight are not included in the blade dynamics calculations. However, if the dynamics can be determined by alternate methods and, if the motion can be reasonably represented by mode shapes in CAMRAD, then the motion can be prescribed as indicated above.

- New vortex/wake modeling was developed to more accurately reflect the relationship between the blade loading details and the wake (structure and position) than was previously done in CAMRAD. The model defines and locates up to two tip-region 'rolled-up' vortices in the rotor wake. In the following sections, the status of this modeling is detailed.

- The flow curvature effects of the windtunnel environment and the shape of the test stand fuselage (or a flight vehicle fuselage) can now be accounted for in the rotor trim and wake geometry. The way the effect is applied is described in a following section.

- A CFD interface is provided to allow the use of the external CFD code FPRBVI (in lieu of the use of HIRES) to calculate the high resolution loading which is needed by the noise code. Here, elastic and rigid blade deflection, low resolution wake, and partial angle or inflow information is passed through the interface. A return path can be provided to the trim loop to take advantage of the loading calculated by the CFD code. This is detailed in Reference 2.

HIRES

HIRES determines high-resolution descriptions of the rotor wake, blade motion, and sectional loads. CAMRAD.Mod1 renders a low resolution 10 degree azimuthal determination of the rotor wake and blade motion. HIRES is an extension to CAMRAD.Mod1, rather than a post processor, which follows the trim calculations. HIRES is typically used to compute blade loads at 0.5 (or 1) degree azimuthal steps and 100 (or 75) radial stations. These high temporal (azimuthal) and spanwise resolution blade loads are obtained by recomputing the wake velocity influence coefficients for recalculated blade motion and interpolated wake geometries (including both tip and secondary vortices) at each azimuthal step. In the interpolations, the vortex elements are allowed to convect downstream with the induced flow in a linear fashion between the low resolution vortex end points. HIRES smoothes the

straight line segmented wake elements of CAMRAD.Mod1 in order to prevent non-physical irregularities in the high resolution sectional loading. The smoothing is accomplished by breaking each 10 degree resolution segments into several segments when the blades are nearby.

The Beddoes[16,17] indicial aerodynamic blade-response modeling employed in HIRES is valid for arbitrarily small temporal steps and impulsive loading. This method is discussed in a following section. The original CAMRAD aerodynamics may be alternately employed to define the high resolution loading. However, the original near-wake model developed by Johnson is valid for only low-resolution, low-frequency, loading. Still, a new lattice aerodynamic model for the near-wake, that is consistent with the original Johnson approach and which is valid for an arbitrary step, has been implemented.

WOPWOP

The rotor acoustic prediction code used is WOPWOP[3], which implements the acoustic formulation 1A of Farassat[4]. This formulation is a time-domain representation of the Ffowcs Williams and Hawkings equation[18], excluding the volume source or 'quadrupole' term for subsonic flow. The input to WOPWOP includes the rotor blade geometry, as a function of span and chord, and the rigid articulated rotor blade motion for flap, lead-lag, and pitch, as a truncated Fourier series (comprised of a constant term and up to two harmonics). The blade loads can be defined over the blade surface, but for use with HIRES the input is compact loading at the quarter chord. For the acoustic predictions presented in this paper, the constant and first harmonic of blade motion predicted by CAMRAD.Mod1 is used. The sectional lift and drag loading from HIRES were defined at either 0.5° (or 1°) of azimuth and 100 (or 75) spanwise stations.

Aerodynamic Modeling Methods

Indicial Aerodynamic Model

The indicial models of Beddoes[16,17] are based on the classical treatment of airfoils in arbitrary motion, but were generalized empirically using experimental and CFD results. The analyses account for uniform and non-uniform compressible inflow, including inflow variations from close blade-vortex encounters, trailing edge separation, dynamic stall, blade pitching and plunging, and the influence of the local three-dimensional near-wake shedding. Blade load response is calculated from a cumulative superposition of responses to individual time step changes in inflow angle. The modeling is in two parts. One is the non-circulatory unsteady loading which has a rapid compressive response to inflow disturbances. The other is the circulatory loading which has both unsteady and steady state components. The circulatory loading depends on the formation of the blade's shed wake, which develops in response to flow disturbances, and is, thus, low frequency in character.

The aerodynamic calculations in HIRES are accomplished in a post-processing program. The program is given the high resolution definition of the far-wake (not including the blade's near wake) induced velocity over the rotor disk. The induced velocity due to the blade's near-wake is determined by a model of Beddoes[17]. The high resolution lift, drag, and pitching moment are calculated along with the above near-wake influence. The lift and drag are then used in WOPWOP to calculate the noise.

A modification was made to Beddoes' non-circulatory response "shaping" function[16], involved in the integration of gust upwash over the chord, to emphasize the leading edge region. This interim modification was to reflect the recently demonstrated leading-edge implusive response to BVI[19]. The modification is not detailed here. The use of the original shaping function is an option in the codes.

Vortex/Wake Modeling

The present modeling effort involves the use of the original version of CAMRAD[15]. The later proprietary versions, CAMRAD/JA and CAMRAD II[20,21], have a number of advanced features over the original. Still, those added features do not address the primary aeroacoustic need of predicting the detailed structure and strength of the trailed vortices in the wake that produce BVI noise. Therefore, the original CAMRAD, including the previously discussed improvements and extensions in attaining CAMRAD.Mod1, is an adequate base for establishing the vortex modeling. Still, as will be indicated in the upcoming sections, the eventual inclusion of the capability of multiple free-wake trailers, such as in CAMRAD II, will be highly desired in future noise prediction codes.

Features of Original CAMRAD Vortex Model - The Scully[15,22] far-field wake model in CAMRAD consists of a free-wake tip vortex and a prescribed inboard wake. The inboard wake in each is represented by pairs of shed and trailed line vortices, which are laid

out by the blades at 10° (or 15°) azimuthal steps and whose geometry and motion in the wake are then prescribed.

Figure 2 illustrates the "far-field" tip vortex model for a particular azimuthal region – the inboard wake is not shown. This is a 'far-field' model, meaning that it is the tip vortex as viewed from another blade, not the blade trailing the vortex (which sees a more distributed 'near-field' shed and trailed wake pattern). The tip vortex consists of a connected series of straight line segments that convect downstream under the influence of the mean and induced flow. The circulation over each segment is linearly varied between the segment end points. The values of circulation at the end points are set equal to the blade's maximum positive bound circulation $\Gamma = \Gamma_{+max}$ at each of the 10° azimuthal steps.

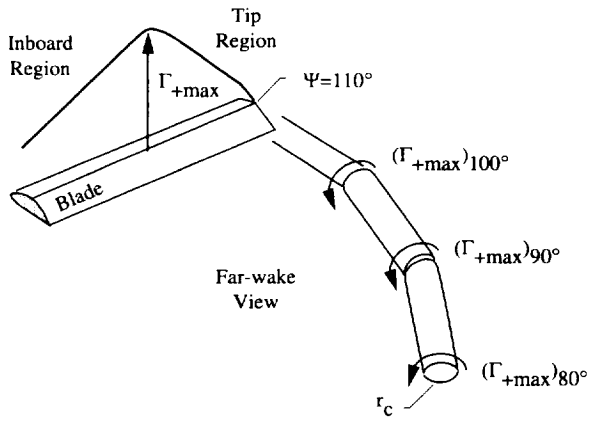

Figure 2: CAMRAD model of far-wake tip vortex trailed from rotor blade.

The swirl velocity v associated with the vortex elements are defined in 3D, but, for illustrative purposes, its 2D limit is

$$v = r\Gamma / 2\pi(r^2 + r_c^2) \qquad (1)$$

where r is the distance from the vortex and r_c is an estimated viscous core radius. This is taken to approximately model the viscous core behavior for 'real' vortices[23] rather than that of an idealized inviscid vortices, where $v = \Gamma / 2\pi r$. Equation (1) is the so-called 'Scully' vortex. The cores of the linked vortices are all taken as the same value, r_c.

Vortex Multi-core Roll-up Modeling Approach - The present approach incorporates elements of the Betz[25] inviscid roll-up method for trailed vorticity from fixed wings. For each blade azimuth station, the bound circulation distribution is used to define and locate an axisymmetric tip vortex with a circulation distribution dependent on the distance from its center. The calculations also define and locate a 'secondary' vortex, which is inboard of the tip vortex, when certain criteria dictate multiple vortex shedding. The present analyses is limited to these two tip region vortices and will not address any additional tip region vortices or the present inboard wake treatment. A blade flap design with two inboard edges, for example, would not be fully modeled in the present analysis.

Figure 3 illustrates the model of the structure of the far-wake vortices which depend on the bound circulation distribution at each blade azimuth station. The vortices shown are taken as fully-developed; the intermediate rolling-up process and aging are not modeled. The phase-in motion of the tip vortex in shifting from the tip to its final inboard position $\bar{y}_t$, as well as the mutual influence of the tip and secondary vortices on themselves, are treated subsequently. The blade tip region is shown with a bound circulation distribution Γ over the spanwise direction y, where $y = 0$ at the tip. The calculations, to be described, define (up to) two fully-rolled-up vortices which are positioned at $\bar{y}_t$ and $\bar{y}_s$, respectively for the tip and secondary vortices. The tip vortex circulation distributions, are defined radially out from the center of the vortex. These distributions are calculated to be (r_t, Γ_t) and (r_s, Γ_s), where Γ_t and Γ_s are the total tip and secondary circulations contained within radii r_t and r_s, respectively. It is desired to use a far-wake algorithm which employs a multi-core model of superimposed single core vortices to attain $(r_t, \Gamma'_t)_p$ and $(r_s, \Gamma'_s)_p$ distributions. These values are to be defined at vortex radial distances from the center: r_p, where p = 1, 2, ..., P (P=9 is typical). The circulations assigned to each element vortex of core radius r_p must be $(\Gamma'_t)_p = (\Gamma_t)_p - (\Gamma_t)_{p-1}$ and $(\Gamma'_s)_p = (\Gamma_s)_p - (\Gamma_s)_{p-1}$. The most inner core radii, $(r_t)_{p=1}$ and $(r_s)_{p=1}$, represent approximate viscous core radii. Two methods can be used for defining these. One is to use a constant minimum-r_c that one may expect for a particular rotor. The other is to use an empirical model for this radius (a model is to be presented in a later section). The corresponding circulations, $(\Gamma'_t)_{p=1}$ and $(\Gamma'_s)_{p=1}$ (as are $(\Gamma'_t)_p$ and $(\Gamma'_s)_p$ in general), are determined from the calculated $(r_t, \Gamma_t)$and (r_s, Γ_s) distributions. The remaining outer cores at $(r_t)_{p>1}$ and $(r_s)_{p>1}$ contain the remaining circulation of the

respective rolled-up vortices. Spacing of these outer cores can be fixed at set radii as long as the spacing sufficiently defines the circulation distribution.

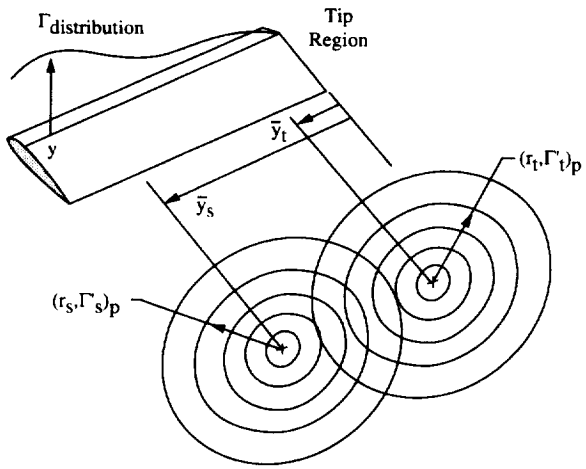

Figure 3: Illustration of multi-core model of rolled-up tip and secondary vortices from tip region. Each are off-set from tip by the distances $\bar{y}_t$ and $\bar{y}_s$, respectively.

The above definition of the multi-core concept allows one to match nearly arbitrary bound circulation distributions to trailed vortex circulation distributions. It is seen that although some choices can, optionally, be made in the code to define the inner core radii, the importance of the core radii as a tuning parameter is significantly reduced compared when the single core model is used.

The details of constructing the multi-core vortex involve the superposition of vortex elements. Based on a Betz[24] concept for a purely inviscid vortex roll-up, one would use the swirl velocity profile modeling for each tip vortex element as, in its 2D form,

$$\begin{aligned} v &= 0 \qquad \text{for} \quad r < (r_t)_p \\ v &= \Gamma_t' / 2\pi r \quad \text{for} \quad r \geq (r_t)_p \end{aligned} \tag{2}$$

and the same for secondary vortex, with s replacing t. However, with viscosity, a finite core is attained and there is a loss or diffusion of vorticity. Because of this and a need to have a functional smoothness to the velocity profile, we use the following modeling for each tip vortex element,

$$v = \frac{r\Gamma_t'}{2\pi(r^{2n} + (r_t)^{2n})^{1/n}} \quad \text{for all r} \tag{3}$$

and the same for secondary vortex, with s replacing t. Here, n is an integer. This velocity modeling[25,26] renders the Scully profile when n=1 and the solid core (or Rankine) vortex model when n approaches infinity. The Scully profile attains only 0.5 of an ideal inviscid vortex circulation at r_c, but is a smooth function of r, and the Rankine profile has the full ideal vortex circulation at r_c, but has a discontinuous slope at r_c. With n=2, the velocity attained is 0.707 of the ideal inviscid case at r_c. The following summation is the velocity description for the tip vortex, in its 2D form

$$v = \sum_{p=1}^{P} \frac{r(\Gamma_t')_p}{2\pi(r^{2n} + (r_t)_p{}^{2n})^{1/n}} \tag{4}$$

and is the same as above for the secondary vortex, but with s replacing t. In the present paper, n=2 was found to represent a reasonable balance between the functional smoothness required in the swirl velocity definition and the circulation values attained. In a following section, this choice in Equation (4) is shown to reasonably match v values for measured vortices.

Figure 4 illustrates how the vortex definitions are employed in the far-wake modeling. A blade is shown at six advancing-side azimuthal locations where the

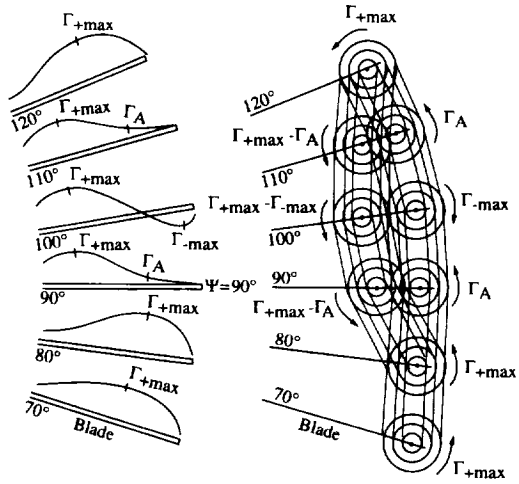

Figure 4: Multi-core vortex elements connected at corresponding radii to show how azimuthal elements are structured. The circulation values shown are those at outer core of each multi-core vortex.

loading distribution changes from high tip loading at 70° and 80°, to negative tip loading at 100°, and back to high tip loading at 120°. The corresponding bound circulation distributions are shown. To the right in the figure, multicore-vortex-patterns for the resultant tip and tip/secondary vortex pairs are seen to be connected at corresponding vortex radii. The combined strengths of the vortices at each azimuth should be the maximum bound circulation Γ_{+max} at that azimuth. This illustration is symbolic in that the fully-rolled-up vortices are shown at locations $\bar{y}_t$ and $\bar{y}_s$ on the blades (represented by lines) rather than showing their translated positions, downstream in the flow. Also, in applying this approach to rotors, the bound circulation distributions such as shown in Figure 4 must be modified by a weighting function due to the rotation of the blade, to be later discussed.

Modified Betz Roll-up Modeling - The present modeling is based substantially on the analyses of Donaldson and Bilanin[27] and Bliss[28] and the theory of the Betz[24] roll-up model of a trailing vortex sheet from fixed wings. The analysis in this section does not account for fact that the blade is rotating. This is dealt with in the following section. The Betz type modeling here is adapted for the rotor problem in a manner which is efficient and compatible with the wake in CAMRAD. The basic tip roll-up model is illustrated in Figure 5, where unlike Figure 3, the inviscid rolling-up process is illustrated. The vortex sheet has a singular edge at the tip which rolls-up and forms the center of the vortex

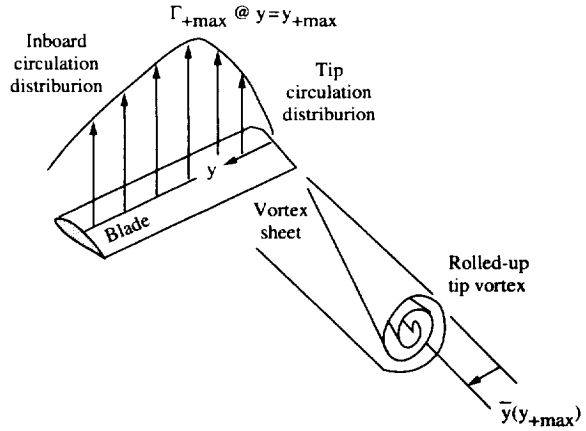

Figure 5: Illustration of tip vortex physical roll-up process.

core. The rolled-up region is composed of spiral turns, which wind tighter and tighter downstream while collecting vorticity from along the blade from the tip at y=0 up to $y = y_{+max}$, where $\Gamma = \Gamma_{+max}$. The bound circulation inboard of $\Gamma = \Gamma_{+max}$. This Γ_{+max} leads to an inboard vortex of opposite rotation, which is not shown or dealt with here - but is treated in CAMRAD.Mod1 by a prescribed inboard vortex. A key equation in the present model is that of the centroid location of the vorticity between the tip and a radially inboard location y. This is

$$\bar{y}_t(y) = \frac{1}{\Gamma(y) - \Gamma(0)} \int_0^y \frac{d\Gamma(\eta)}{d\eta} \eta d\eta = \frac{1}{\Gamma(y)} \int_0^y \frac{d\Gamma(\eta)}{d\eta} \eta d\eta \quad (5)$$

where the subscript t signifies the tip vortex. When the integral extends to $y = y_{+max}$ and all the vorticity is rolled-up, the tip vortex center in the y direction is $\bar{y}_t = \bar{y}(y_{+max})$. An illustration of terms of this equation is given in Figure 6. It should be mentioned that the above equation and others in this paper have a somewhat different appearance than those of References 27, 28, and 24, because their direction of integration is opposite, with y = 0 at $\Gamma = \Gamma_{+max}$. Another key equation is a statement of Kelvin's theorem, which is a conservation of vorticity requirement, that the circulation of each sub-interval of the sheet between y=0 and y, be related by

$$\Gamma(y) = \int_0^y \frac{d\Gamma(\eta)}{d\eta} d\eta = \int_0^r \frac{d\Gamma(\lambda)}{d\lambda} d\lambda = \Gamma(r) \quad (6)$$

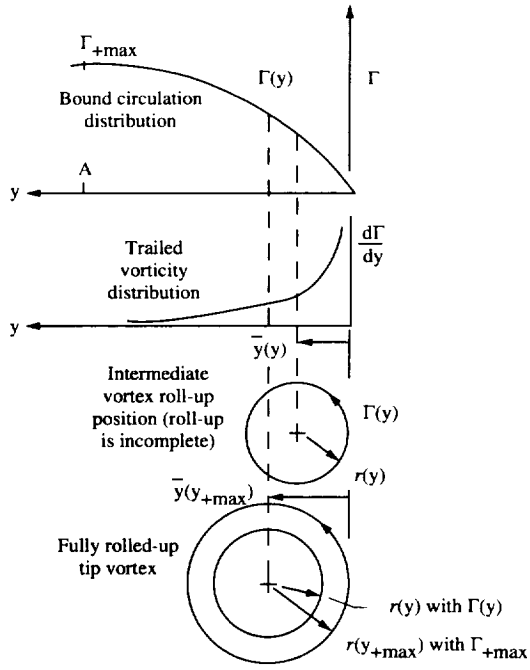

Figure 6: Relationship between bound circulation, vorticity trailed, and roll-up radial strength for single tip vortex roll-up.

Reference 27 describes how this leads to a surprisingly simple result (or interpretation, Ref. 28) that $r = \bar{y}(y)$. This means that the value of the circulation at position y equals the circulation at the radial distance r in the fully rolled-up axisymmetric vortex. Therefore, at intermediate radial positions

$$r = r(y) = \bar{y}(y) \tag{7}$$

where $\Gamma(r) = \Gamma(y)$. And, at the outer edge of the tip vortex,

$$r = r(y_{+\max}) = \bar{y}(y_{+\max}) = r_t \tag{8}$$

where $\Gamma(r) = \Gamma(y_{+\max}) = \Gamma_{+\max} = \Gamma_t$. The resultant relationships between blade loading and the trailed vortex is illustrated in Figure (6).

The above is a valid approach as long as the calculated value of $r(y)$ increases monotonically with successive stepwise y integrations using Equation (5). However, when the tip is irregularly loaded between y=0 and $y_{+\max}$, $r(y)$ and y may not be single valued functions of one another. This behavior can be avoided if a roll-up of a second vortex is assumed and the vorticity divides itself at $y = A$ where such behavior first occurs. Figure 7 shows an example of such a loading which leads to multiple vortex trailers. Calculation of $\bar{y}(y)$ stops at $y = A$, with a centroid of vorticity value of $\bar{y}_t$, and the tip vortex is defined with outer radius r_t and strength Γ_t. The secondary vortex contains the vorticity between A and $B = y_{+\max}$. The

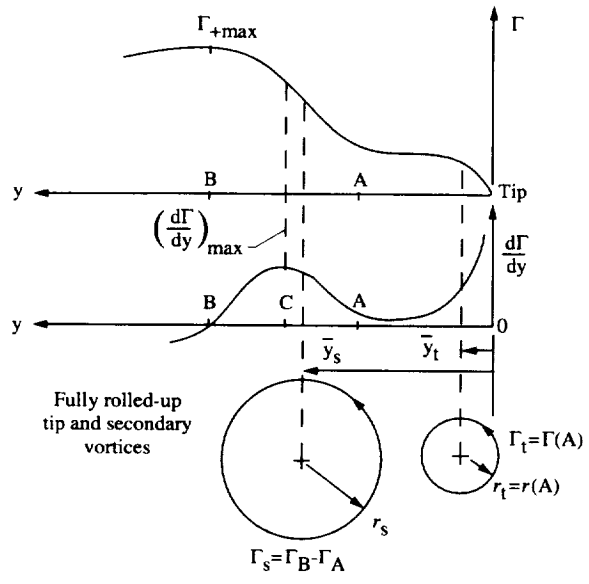

Figure 7: Relationship, as in Fig. 6, but for one positive tip vortex and one positive secondary vortex.

following method for constructing the secondary vortex stays within constraints suggested in Reference 27, where the subject is discussed. The centroid of vorticity $\bar{y}_s$ is taken to be the resultant position of the vortex, and is determined by

$$\bar{y}_s(y) = \frac{1}{\Gamma(B) - \Gamma(A)} \int_A^B \frac{d\Gamma(\eta)}{d\eta} \eta \, d\eta \tag{9}$$

We shall define the origin of the roll-up to be at the location $y = C$, for which the slope $-|d\Gamma / dy|$ is maximum. To form the vortex, the vorticity is modeled as being collected about the origin $y = C$. The centroid $\bar{y}_s$ serves as the origin if $-|d\Gamma / dy|$ is not strongly defined. The relationship between the vortex radius r and Γ is taken to be

$$\Gamma(r) = \int_C^{C+r''} \frac{d\Gamma}{d\eta} d\eta + \int_{C-r'}^{C} \frac{d\Gamma}{d\eta} d\eta = \int_{C-r'}^{C+r''} \frac{d\Gamma}{d\eta} d\eta \tag{10}$$
$$\Gamma(r) = \Gamma(C + r'') - \Gamma(C - r')$$

In this equation, the relationships between r, r', and r'' are given by

$$\begin{aligned} r &= r' \quad \text{for} \quad r' \geq A \\ r &= A \quad \text{for} \quad r' < A \\ r &= r'' \quad \text{for} \quad r'' \leq B \\ r &= B \quad \text{for} \quad r'' > B \end{aligned} \tag{11}$$

Equation (11) and the use of r' and r'' in Equation (10) represent requirements, which were not dealt with in Reference 27, in order to account for situations where C is not centered between A and B.

It is seen then, for this secondary vortex, that r is not a quantity determined by a weighted integration over y as in Equation (5), but is the appropriate spanwise distance on either side of the maximum $-|d\Gamma / dy|$ location required to capture its respective vorticity. Equations (10) and (11) show that vorticity is collected from both directions until A (or B) is reached; thereafter, collection from only the other direction is continued until B (or A) is reached. The final radius and strength of the secondary vortex is then $r_s = B - C$ (or $C - A$) and $\Gamma_s = \Gamma_B - \Gamma_A$.

Figure 8 shows another bound circulation distribution which leads to multiple trailed vortices in the tip region. Here, however, the tip vortex is negative in rotation due to negative tip loading. This situation is not treated in References 27, 28, and 24. But, by

logical extension, the procedure taken here is to calculate r_t and Γ_t the same way as above, including the criteria to define the point A. The secondary vortex, however, should contain the vorticity between Γ_{+max} and Γ_{-max} (the most negative circulation in the near tip region). This means that B equals y_{+max} and A now equals y_{-max} in using Equations (8), (9), and (10).

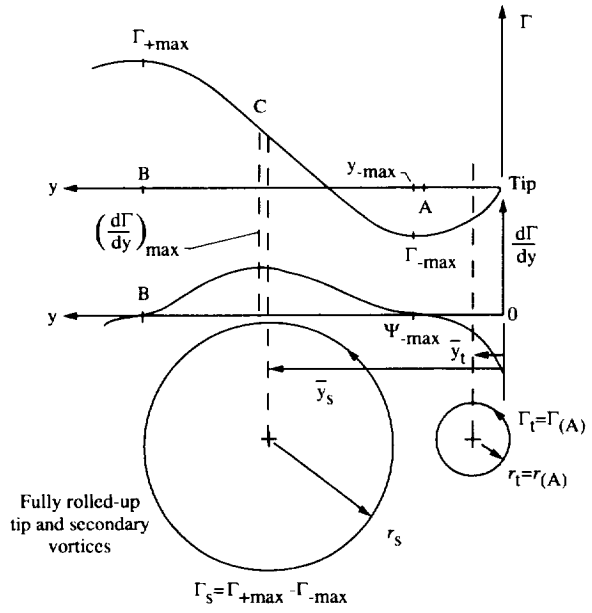

Figure 8: Relationship, as in Fig. 6, but for one negative tip vortex and one positive secondary vortex.

A comparison of Figures 7 and 8, illustrates some of the similarities and differences between these two circulation distribution cases. It is seen in Figure 8 that that if A is found to be less than y_{-max}, some vorticity would be lost in the calculations. It is assumed that the potential error due to this omission is negligible or, at least, commensurate with other limitations of the overall methodology. One such limitation is the secondary vortex calculation procedure which presupposes a single vortex roll-up from the point A to y_{+max}, where in reality multiple vortices may occur.

Fat Core Calculation and Vortex Segment Stretching Model - The above roll-up modeling would apply directly to a non-rotating blade in uniform flow. But with rotation and the fact that the blades can operate within the wakes of preceding blades in their rotation, the bound circulation has to be conditioned prior to the roll-up calculations. The first effect to be accounted for is illustrated in Figure 9, which shows spanwise bound circulation distribution which was calculated in CAMRAD.Mod1 for a windtunnel rotor test case (from the HART test to be discussed). The particular blade azimuth position is Ψ=140° in the second rotor

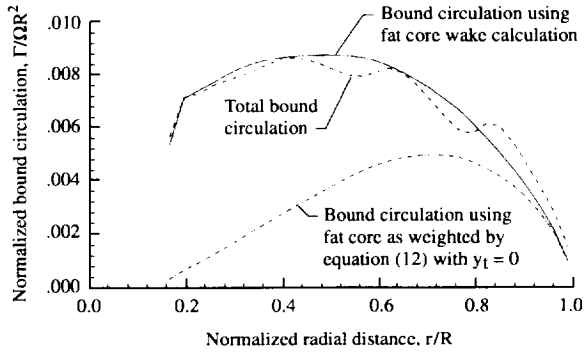

Figure 9: Bound circulation distribution for a rotor blade at 140° azimuth and two steps of modifications that are required prior to each roll-up calculation.

quadrant, where near-perpendicular vortex interactions occur which cause noticeable spanwise circulation 'hump and valley' type variations. These variations can have significant impact on the roll-up calculations. It is hypothesized here that the variations that relate to these vortex interactions relate to local spanwise load variations and subsequent releases of vorticity directly back into the encountered vortices as the blade passes. Under this hypothesis, these circulation variations would not contribute to the formation of new vortices released into the wake. To remove these variations prior to the roll-up calculations, the loads were recomputed, using large core sizes for the vortices in the wake. The resulting bound circulation distribution, also shown in Figure 9, is seen to be smooth. A fat single-core radius of 0.3R was used, which was found to smooth the distribution adequately while maintaining the influence of the induced flow of the wake and the contribution of the uniform inflow and the blade motion.

Further conditioning of the bound circulation distribution is required to account for the fact that the blades are rotating during forward flight. Figure 10 shows a rotating-blade tip vortex with straight line segments being emitted at $\bar{y}_t$. To illustrate a concept, vortex line filament segments, signifying vorticity trailed from locations y, are shown outboard and inboard of $\bar{y}_t$. Each segment length depends on the

spanwise location for a given azimuth step size and the rotational and inflow velocity at y. Each filament segment has an induced field velocity of $\delta v = \delta\Gamma\delta l / r$. In the roll-up calculations, the vorticity segments are drawn to and entrained in the vortex at $\bar{y}_t$, with the

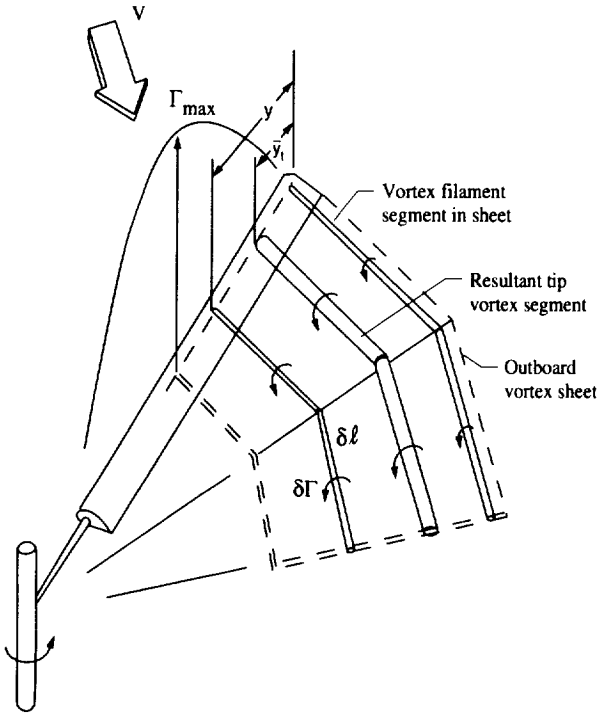

Figure 10: Rotor blade with line segment modeling of trailed vorticity due to blade Γ distribution.

length now defined at $\bar{y}_t$. When this is done, stretching (or compression) of the vorticity must occur in proportion to the ratio of its original segment length to its new length at $\bar{y}_t$. This serves, in principle, to maintain the same δv contribution at an observer at r in the wake. Therefore, weighting factors need to be applied to the bound circulation distribution in connection with the roll-up calculations. The weighting factor for the bound circulation distribution producing the tip vortex is

$$\frac{(R-y)\Omega + V\sin\Psi}{(R-\bar{y}_t)\Omega + V\sin\Psi} = \frac{(1-y/R)+\mu\sin\Psi}{1+\mu\sin\Psi} \cdot \frac{1+\mu\sin\Psi}{(1-\bar{y}_t/R)+\mu\sin\Psi} \quad (12)$$

The effect is to increase the Γ contribution of the filaments outboard of $\bar{y}_t$ and to decrease those inboard of $\bar{y}_t$. The calculation procedure is to first modify the Γ distribution by multiplying the first term of the right-hand expression of Equation (12). The result of this weighting is illustrated in Figure 9. Note that this gives a distribution which is now proportional to the sectional lift rather than circulation. After performing roll-up calculations using this weighted Γ distribution (where $\bar{y}_t$ is determined), the resulting calculated strengths of each multi-core vortex element are then multiplied by the last term of the right-hand expression of Equation (12). For the secondary vortex, the procedure is the same as above with $\bar{y}_s$ replacing $\bar{y}_t$ in Equation. (12).

Vortex Geometry and Spin Model - The present use of the Scully free-wake model[22,15] in CAMRAD.Mod1, puts constraints on the way that the wake geometry can be defined. The approach taken is to first run the Scully free-wake code without modification to the CAMRAD method (using the maximum bound circulation without weighting or stretching). And to then make alterations in the resulting wake geometry during the influence coefficient calculations. The new tip and secondary vortices are both tagged to the free-wake tip vortex determined from the Scully wake model. For every blade azimuth location, the apparent origins of the tip and secondary vortices are, each, from positions $\bar{y}_t$ and $\bar{y}_s$ on the blade rather than at the tip itself at y=0. The geometric path that the vortices follow in convecting downstream are that of the Scully tip result. The vortex elements in the wake are therefore shifted to give the new rolled-up positions for the vortices. For the purpose of giving a transitional smoothness, an allowance is made for the tip vortex to phase-in to its new rolled-up position. At present, the origin of the tip vortex position is linearly varied from y=0 to $\bar{y}_t$ (full phased-in location) over a period of one revolution. No phase-in period is given for the secondary vortex with $\bar{y}_s$ being the starting and final origin.

With the lack of a free-wake code which includes both the tip and secondary vortices, an ad hoc model was developed to account for the mutual influence of the two vortices. A spin model was implemented which spins and translates the two vortices at rates and directions which are determined by their origins ($\bar{y}_t$ and $\bar{y}_s$ on the blade) and their respective circulation distributions. To illustrate—the two vortices of opposite sign at Ψ=100° in Figure 4 would both translate upward and rotate about the pair's centroid of circulation. If the secondary vortex were stronger, the tip vortex would initially rise above the secondary. The model accounts for the other combinations of circulation direction. The model is locally 2D with each vortex seeing only its pair at each azimuth. The extent to which this model reflects real 3D behavior would depend on the particular rotor case. Of course,

the biggest limitation in the model may be that the influences of the other parts of the wake are not included.

Windtunnel and Fuselage Corrections - As previously mentioned, the effects of the windtunnel environment and the fuselage can be accounted for in the rotor trim and wake geometry by defining the related flow distortions on the rotor disk. The flow corrections are determined using separate codes. A fuselage panel code[29] determines the flow curvature due to the shape of the nearby fuselage. It does not account for aerodynamic interference, or 'partial ground' effects, between the fuselage and rotor. The windtunnel wall corrections are determined by a recently-developed Langley code[30], which has been a subject of a validation study[31].

In CAMRAD.Mod1, a 'velocity correction' vector field from a sum of the windtunnel and fuselage effects are determined over a plane which includes the rotor. The rotor aerodynamic portion of the trim incorporates this velocity correction field as a mean and a residual distortion, in order to (1) redefine the 'flight condition' based on a mean correction and to (2) then add the distortion field to the velocity distribution over the rotor disk. In this aerodynamic trim, both the tip and secondary vortices are properly accounted for in the loading calculations.

In the wake portion of the trim, the presently used Scully free-wake model does not permit the addition of an external velocity field. Therefore, a calculated wake distortion is simply added to the resulting free-wake geometry, in order to obtain a corrected wake geometry. This corrected wake distortion is determined in a separate time step analysis (outside of trim and CAMRAD.Mod1) of induced motion through the 'velocity correction' field. These are input as incremental distortions at each wake endpoint location. The tip and secondary vortices are then positioned, as discussed in the last section, relative to these wake locations. This is done for all iterations between the free-wake geometry calculations and aerodynamic trim.

Predictions And Experimental Comparisons

HART Program

As mentioned, HART was a multi-national cooperative program conducted in the open test section of the German-Dutch Windtunnel (DNW). The DLR rotor model test stand is shown mounted on the DNW sting in Figure 11. The rotor is a 40-percent dynamically and Mach scaled model of the BO-105 main rotor. The model is 4m in diameter, four-bladed, hingeless, and has a pre-coning of 2.5° at the hub. The rectangular planform blades have a chord of 121 mm and a −8° linear twist. The noise is measured using a 11-microphone traverse, positioned 2.3 m underneath the rotor plane, that obtained data at each 0.5 m

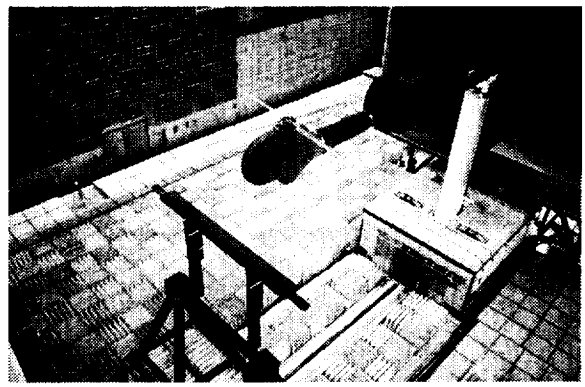

Figure 11: HART configuration - DLR model rotor and in-flow microphone traverse in the 6m by 8m open test section of the DNW.

streamwise position. More details are reported by Splettstoesser, et al.[8]. The HART test conditions considered here are confined to five cases (most of which has been extensively reported[8,9,10,12,13,14]). In each, $\mu = 0.15$, $C_T = 0.0044$, and $\Omega = 1040$ rpm ($M_H \approx 0.64$), where the hub lateral and longitudinal moments are trimmed to zero. Baseline non-HHC cases were at shaft axis angles of $\alpha_s = 3.8°$, 5.3°, and 6.8°, referred to as BL (3.8°), BL (5.3°), and BL (6.8°). For $\alpha_s = 5.3°$, two cases are considered of 3P-HHC (frequency of three HHC cycles per rotor revolution, see Reference 8) with HHC amplitudes of 0.85°. The 3P-HHC control angles were 296° and 177° for the conditions referred to as HHC-MN (for minimum noise) and HHC-MV (for minimum vibration), respectively.

In CAMRAD.Mod1, the rotor was trimmed to zero-moment for the cases above. The elastic blade motion, as calculated by strain gage measurements, was used instead of the CAMRAD dynamics model. The trimming to C_T and moment was accomplished through the determination of the collective and cyclic control angles. The windtunnel and fuselage thickness-related corrections for flow and wake distortion were included in the trim loop. For the multi-core vortex roll-up model in the code, a set of 9 core radii was established, as well as a semi-empirical model for the inner 'viscous core' radius. These corrections and multi-core vortex model application are first described and then the wake and noise results are shown.

Flow corrections - The calculated distributions of the windtunnel and fuselage flow-angle corrections, for HART cases in this report, are shown in Figure 12. The contours are of the flow angle between the tunnel-plus-induced horizontal velocity, and the vertical induced

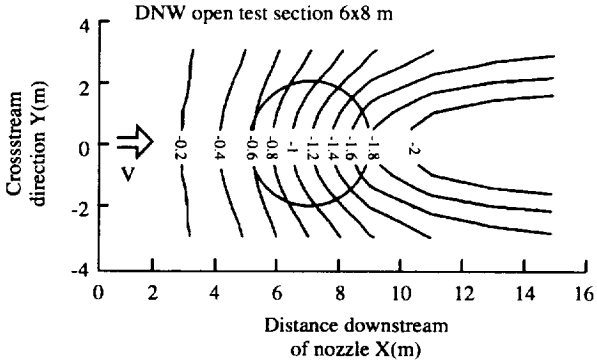

(a) Windtunnel corrections for μ=.15 and C_t =.0044.

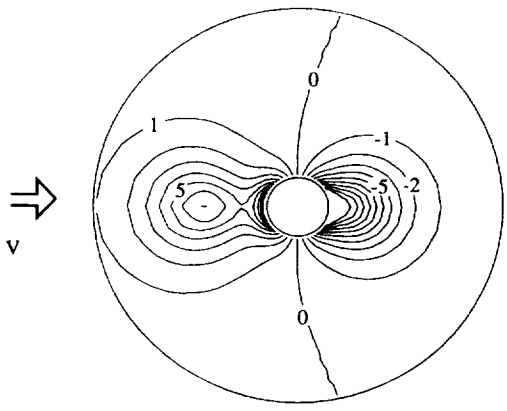

(b) Fuselage corrections.

Figure 12: Flow-angle correction distribution in the rotor disk plane. Angles are given in degrees.

velocity due to tunnel boundaries and fuselage thickness. The fuselage, including the hub dome, is modeled by a potential flow panel method. The total mean tunnel and fuselage correction over the disk is $-1.12° + 0.16° = -0.96° \approx -1°$. In addition to this mean value, the spatial distribution of the correction can be seen to be important in defining the trajectories and orientations of the BVI producing vortices. For example, a vortex that the formed in the second quadrant that leads to a BVI event at about $\Psi \approx 35°$ for the blade, in the first quadrant, may have had its trajectory influenced by an average of $-1°$ flow angle deviation. For this angle, a vortex element convecting downstream at a distance of $1.5R$ would give a total downward deflection of .05 m or .43 c with respect to the blade. For a more upstream BVI at $\Psi \approx 80°$ for the blade, vortices may have been influenced in its trajectory on the average of only about $-0.4°$ with correspondingly less deflection. As previously noted, although the flow corrections due fuselage thickness are accounted for in the analysis, the aerodynamic interference (or partial ground-plane) effects of the fuselage are not. For the present fuselage, this is may not be significant. Another flow effect, not accounted for, is that of the microphone traverse, positioned 2.3 m below the rotor plane. Calculations based on thrust changes when it is underneath the rotor suggest that up to a 0.5° upwash aerodynamic interference effect on the rotor.

Multi-core vortex application - Figure 13(a) and 13(b), for the cases BL (5.3°) and HHC-MV respectively, show the calculated values of centroids of

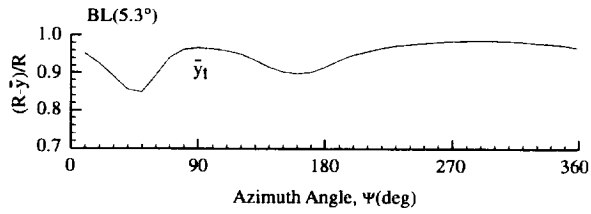

(a) Baseline condition at α_s= 5.3°.

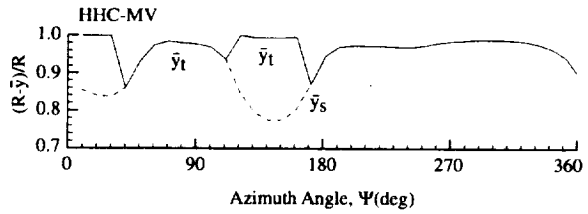

(b) Higher Harmonic Control - Minimum Vibration condition at α_s= 5.3°.

Figure 13: Calculated $\bar{y}$ vs. azimuth.

vorticity as function of blade azimuth position. For BL (5.3°), the blade's bound circulation for all azimuth positions correspond with the case of Figure 6. Thus, only a tip vortex is formed, with its rolled-up position at $\bar{y}_t$. It is seen that, except for the 1st quadrant ($0° \le \Psi \le 90°$), $\bar{y}_t$ is within 0.1R of the blade tip. For HHC-MV, the blade dynamics are such that significant elastic pitch, flap, and lead-lag blade motion occur. This, primarily the pitch motion, causes bound circulation changes that produce the $\bar{y}$ distribution given in Figure 13(b). Multiple vortices are seen to be

released in regions of the 1st and 2nd ($90° \le \Psi \le 180°$) quadrant. These correspond to the case of Figure 8, where negative tip vortices are formed. It is seen in Figure 13(b) that there is a continuity between the tip vortices, of azimuth regions where only single vortices are formed, and the secondary vortices. This is because they are both associated with the maximum bound circulation of the blade — the new tip vortex can be viewed as a 'break-away' from the main wake roll-up.

A semi-empirical model for the inner 'viscous-core' radius was developed based on the calculated $\bar{y}$ values and approximate values for the viscous core radii r_v reported in Reference 8. The radii r_v was determined in regions near BVI locations on the advancing and retreating side. The data was extracted from LDV measurements of the DLR and ONERA teams (whose acquisition methodology is generally described, respectively, in References 32 and 33). For our five cases of interest, Figure 14 shows the values for r_v / R versus $\bar{y}_t / R$ or, alternately, $(y_s - A)/R$ for the secondary vortex. The term A is the calculated

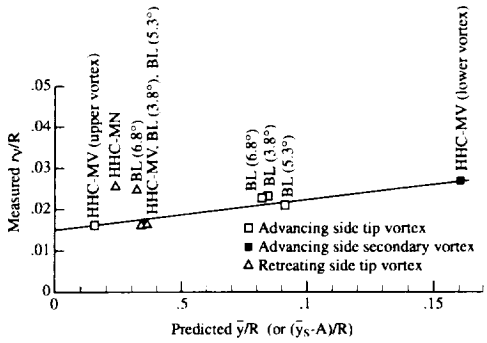

Figure 14: Correlation of measured vortex radii r_v, from Ref. 8, and calculated $\bar{y}$ values.

spanwise separation point of the secondary vortex (see Figures (7) and (8)). Based on the LDV measurement locations and CAMRAD.Mod1 predicted wake geometries (that show apparent vortex origins), $\bar{y}_t / R$ values used were those at Ψ = 140°, for advancing side tip vortices, and 230°, for the retreating side tip vortices. For the secondary vortex case, , $(\bar{y}_s - A)/R$ used was that at Ψ = 130°. The plot shows agreement with a straight line function, with exception at two points. The function is for tip and secondary vortices, respectively,

$$r_v / R = .015 + .075(\bar{y}_t / R)$$
$$r_v / R = .015 + .075(\bar{y}_s - A)/R \qquad (13)$$

It is seen that this viscous-core radius r_v is defined only in terms of the rotor radius R and the distances $\bar{y}_t$ (or $(\bar{y}_s - A)$). These distances may be interpreted physically as radial distances over which the vortices collect vorticity. For heavy loading at the tip, the vorticity is concentrated and $\bar{y}_t / R \approx$ zero. Equation (13) includes whatever effects the age and the upstream wake and blade interactions had on the evolution of the vortices for the particular BVI condition for this model.

Figure 15 shows the inner portion of the radii distribution used in the multi-core vortex model. The $(r_t)_p / R$ and $(r_s)_p / R$ radii were 0.01, 0.0167, 0.0233, 0.03, 0.04, 0.05, 0.07, 0.1, and 0.2. The variable viscous-core radius r_v is determined by Equation (13).

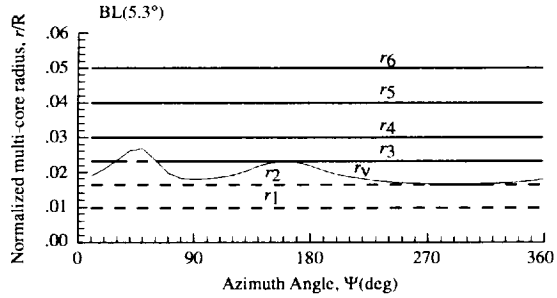

Figure 15: Radii used in multi-core vortex model for BL(5.3°). r_v determined from Equation (13).

It is seen for this BL(5.3°) case that r_v is larger than $(r_t)_{p=1,2}$ over most of the azimuth and larger than $(r_t)_{p=3}$ near Ψ = 50°. Where this occurs, the dashed lines of these radii indicate that the circulation associated with these are now included in the r_v vortex. When r_v is between radii, the r_v vortex includes an interpolated portion of the circulation of the larger-radius vortex. Figure 16 shows the resultant circulation distribution over the azimuth. It is seen that this tip vortex is dominated by the circulation at r_v, although

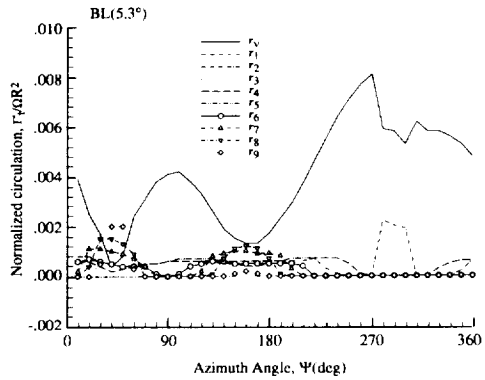

Figure 16: Circulations corresponding to multi-core radii of Figure 15.

other radii contribute, especially in regions of the 1st and 2nd quadrant where loading is less concentrated at the tip and $\bar{y}_t / R$ is large. Figure 17 shows how well the multi-core model matches the measured vortex

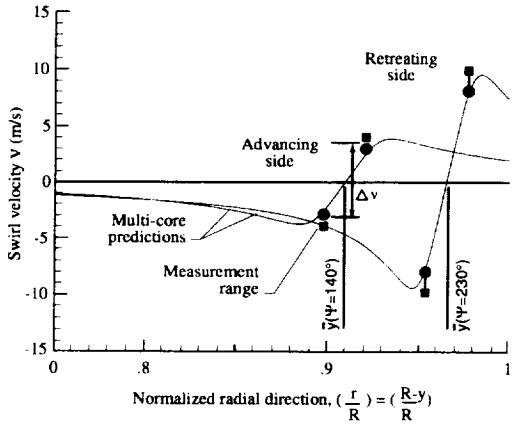

Figure 17: Predicted swirl velocities Δv for vortices originating at Ψ = 140° and 230°for BL(5.3°). Vortices are placed at their respective spanwise origin positions. Measured downstream Δv and r_v values are compared.

results for the BL(5.3°) case. The calculated swirl velocities, for the tip vortices generated at Ψ = 140° and 230°, are shown positioned at their $\bar{y}_t$ values. The measured maximum swirl velocities were estimated in the present study from the LDV data; and are plotted at distances r_v / R (measured value[8]) from $\bar{y}_t$. The measured velocities show a confidence range rather than single points. The range is defined by an uncorrected value of velocity found across the vortex and a larger corrected value. The correction, which is intended to make such a comparison in Figure 17 compatible, is based on assumed vortex properties and orientation of the measured vortex with respect to the LDV cut. In this same light, the measured r_v / R is regarded as uncorrected. Figure 17 shows that the velocity is somewhat over-predicted for the advancing side but well predicted for the retreating side. It is noted that the present choice of n = 2 in Equation (4) does have an effect on the velocity comparison. The alternate use of n = 1 would cause an under-prediction and n = 4 would cause an over-prediction. With regard to core size in Figure 17, the measured viscous core r_v / R is smaller than a so-called 'effective' core size r_c defined by the distances at the peaks of swirl velocities. This appears to be consistent with the method of choosing radii r_v in Reference 8. Table 1 lists comparisons between the velocity differentials Δv between the vortex peaks and between the radii r_c and r_v for the five HART cases. A review of the list shows both under and over-prediction of Δv and a consistent relationship between r_c and r_v. Overall, the agreement is considered quite good and serves to help establish the correctness of the multi-core model .

Results - Wake geometry plots are presented in Figure 18 for the five HART cases. For clarity, with only one blade of the four blades are shown. Predicted and measured[8] tip and secondary vortices are shown as snapshots from above the rotor, in the plan view, and from behind and normal to the blade, in the side view. X is the streamwise direction (positive upstream) and Y is the cross-stream direction (positive on advancing side). Z is the distance from the rotor hub center along the shaft axis (positive above the rotor). The coordinate r is the radial distance along the blade. Figure 18(a) gives results for two blade azimuth positions, at Ψ = 35° and 295°. In Figures 18(b)-(e), only the Ψ = 35° cases are shown. For identification, the vortices are separately numbered for each blade azimuth

Test Condition	Advancing Side				Retreating Side			
	Meas. range Δv(m/s)	Predicted Δv(m/s)	Meas. (Ref.8) r_v/R	Predicted r_c/R	Meas. range Δv(m/s)	Predicted Δv(m/s)	Meas. (Ref.8) r_v/R	Predicted r_c/R
BL (α=3.8°)	4.4 - 5.3	7.0	.023	.026	10.2 - 12.2	20.6	.015	.018
BL (α=6.8°)	6.2 - 7.6	6.9	.023	.024	12.3 - 15.7	19.5	.025	.018
BL (α=5.3°)	5.8 - 6.9	7.6	.021	.026	16.0 - 19.6	18.9	.015	.019
HHC-MN	-	18.8	-	.019	8.9 - 10.7	24.8	.025	.018
HHC-MV (lower vortex)	8.6 - 10.6	4.1	.027	.033	18.8 - 22.5	20.9	.015	.019
HHC-MV (upper vortex)	9.8 - 11.8	10.1	.016	.016	-	-	-	-

Table 1: Comparison of predicted and measured core sizes and swirl velocity difference across vortices for the five HART cases.

case. The measured data shown were obtained from Laser Light Sheet (LLS) method[3,4,8] that determined the vortex position with respect to the blade. In Figure 18, the LLS measured vortex segments were positioned with respect to blade positions from CAMRAD.Mod1. These blade positions are, as mentioned, measured positions based on strain gage data.

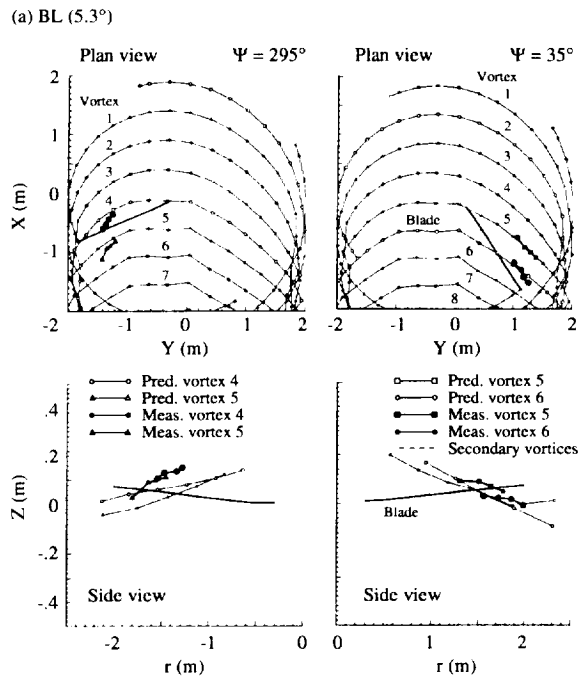

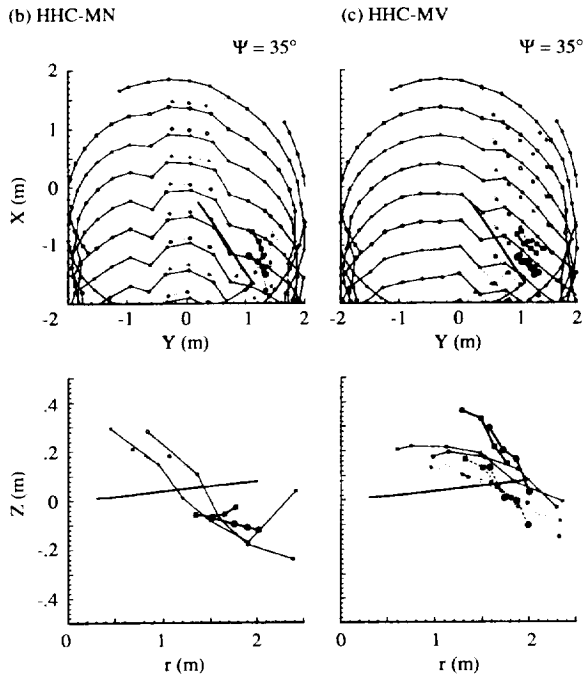

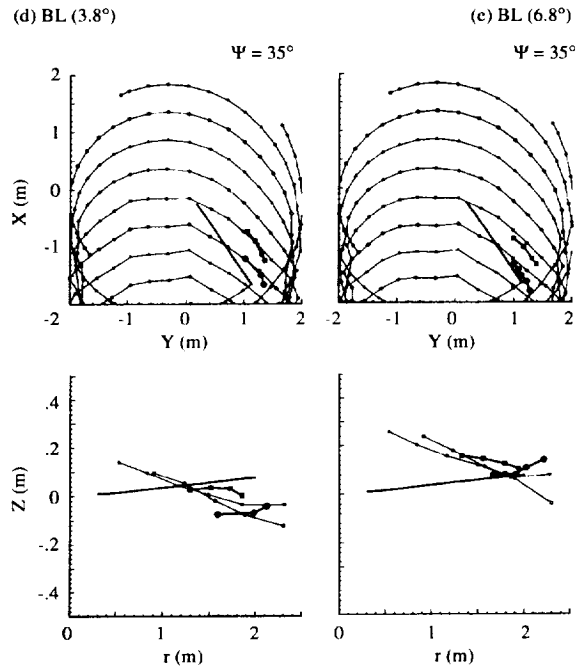

Figure 18: Predicted and measured wake geometry for the HART model of tip and secondary vortices - at instant of time where the blade is at Ψ=35° (or 295°). The top plan view is shown, as well as a side view of several vortex segments from behind and normal to the blade.

The comparisons in Figure 18 reveal generally good agreement. For the BL cases that involve only tip vortices, the streamwise, lateral, and vertical positions of the predictions are much improved over that obtained before the present roll-up model was developed[12]. Additionally, for the HHC cases, the new wake modeling appears to lead to a more detailed understanding of the occurrence of the dual vortex phenomena. For the HHC-MV case in Figure 18(c), the modeling shows that the measured dual vortices on the advancing side are paired above and below by tip and secondary vortices that originate from different blades. A pair of vortices were also identified in the predictions of Reference 14, but the positions and origins were not well defined. The present tip and secondary vortex spin modeling, as mentioned, does not include influences from vortices of different blades. Still, the vertical positioning of the vortices appear reasonably predicted.

Measured and predicted mid-frequency noise contour plots are presented in Figure 19. The rotor tip path is

shown as circles and the flow is from the top to bottom of the figure. The measured contour or 'carpet' plots were determined from microphones of the traverse. The levels are obtained by integrating the noise spectra from the 6th through the 40th blade passage harmonic. The spectra in these frequencies are dominated by BVI noise contributions in these descent cases. All cases show two distinct BVI noise directivity lobes, one each on the advancing and retreating sides. The comparison for BL(5.3°), in Figure 19(a), shows that the maximum levels and directivity of the lobes are generally well predicted. Parts (b) and (c), for the HHC cases with the same nominal flight condition, show noticeable changes in the noise. For HHC-MN, the predictions appear to be capturing the basic trends of the directivity and amplitude changes. For HHC-MV, the shape but not the amplitudes are roughly matched. In part (d), the more vertical orientation of the shaft angle for BL(3.8°), compared to BL(5.3°), produces a forward shifting of the advancing side lobe with a slight drop in level. This observed feature and an amplitude drop on the retreating side is predicted. In part (e), for the more backward shaft tilt of BL(6.8°), the advancing side lobe's shift to the side is predicted.

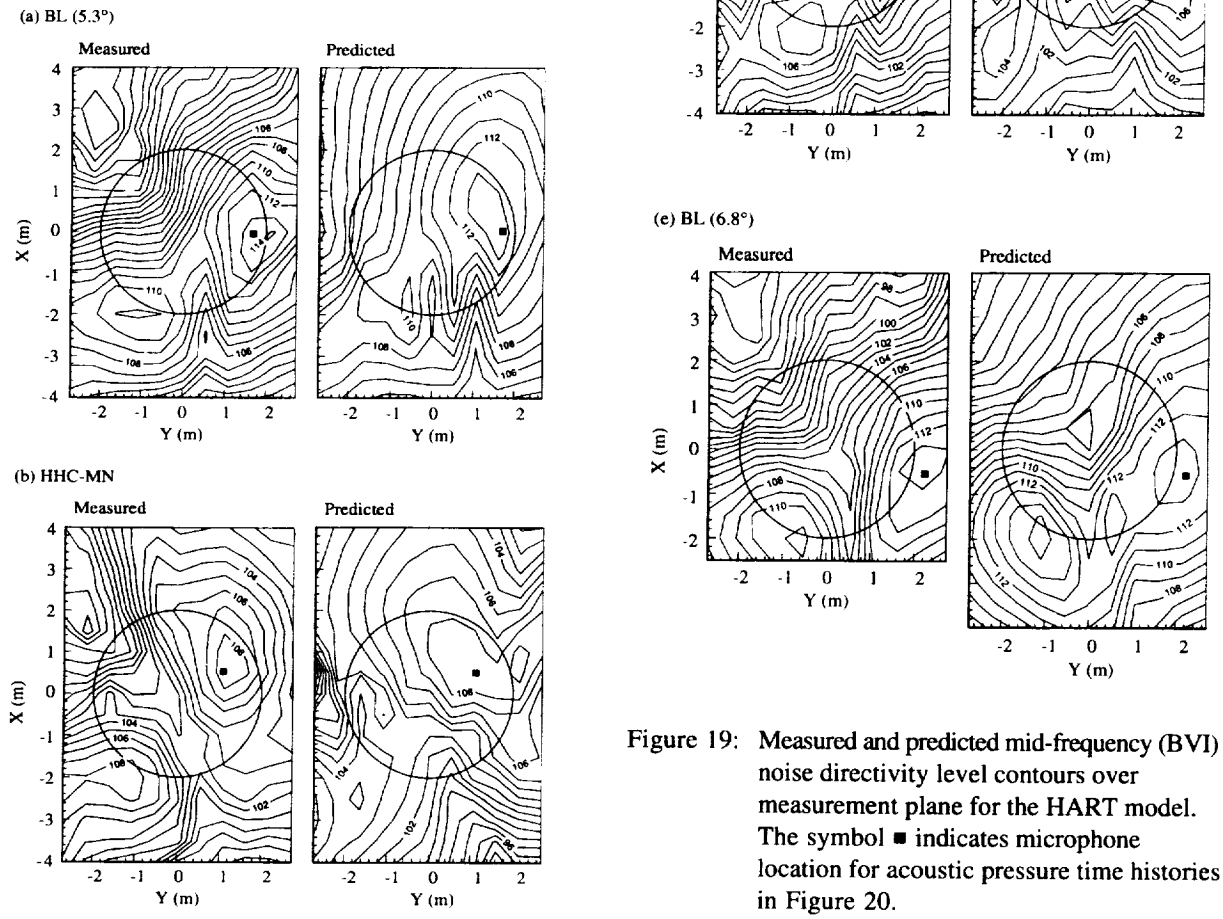

Figure 19: Measured and predicted mid-frequency (BVI) noise directivity level contours over measurement plane for the HART model. The symbol ■ indicates microphone location for acoustic pressure time histories in Figure 20.

Measured and predicted acoustic pressure time histories are shown in Figure 20, for the corresponding conditions of Figure 19. The measured time histories are obtained by averaging data over 30 revolutions. No frequency filtering was done — so the low frequency harmonic noise is included. The microphone locations are on the advancing side BVI lobes. Figure 20 shows that for BL(5.3°), the basic impulsive BVI and harmonic noise characteristics are predicted. With the use of HHC, the character of the noise produced changes drastically. For the HHC-MN case, the large increase in harmonic noise and decreases in BVI noise, compared to the non-HHC BL(5.3°) case, is predicted. For the HHC-MV case, the more moderate increase in harmonic noise, compared to HHC-MN, and the appearance of additional BVI impulses are also seen in the prediction. However, here, the number of the BVI occurrences are not captured. For the non-HHC cases, the basic amplitudes and features of the harmonic and BVI noise are captured, as well as shifts in the BVI impulses.

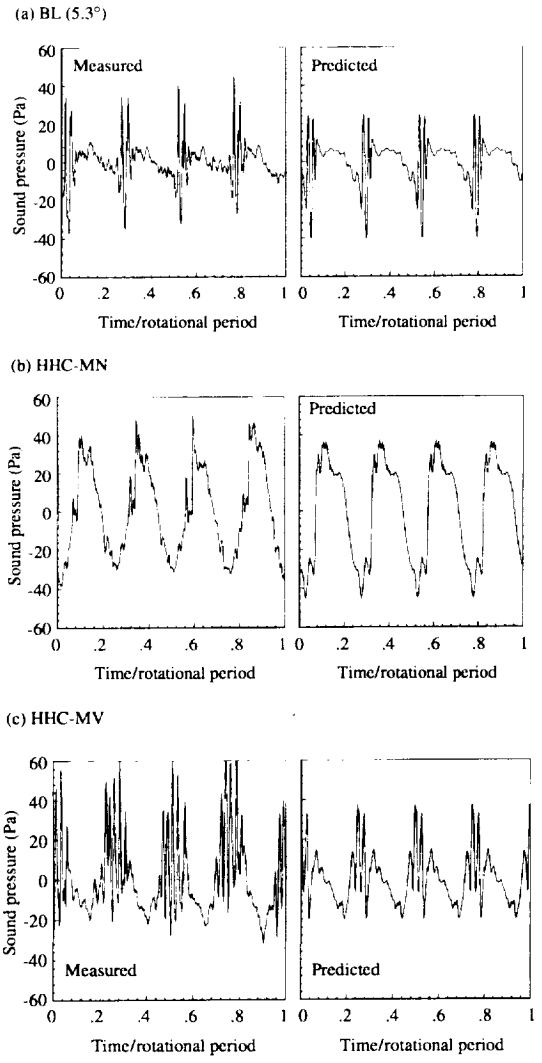

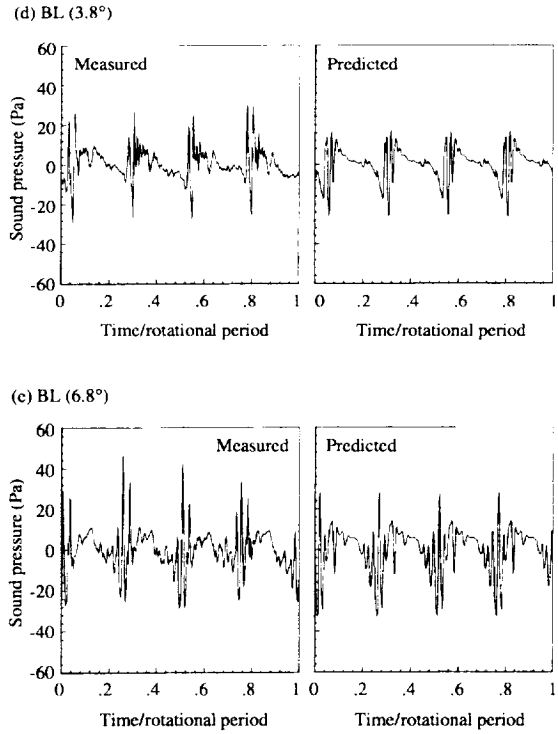

Figure 20: Measured and predicted acoustic pressure time histories for the HART model for microphone locations indicated in Figure 19.

UTC Model Test

The prediction method is now compared to data from a 1989 aeroacoustic test conducted in the DNW[35]. The test was part of the U.S. Army Aerodynamic and Acoustic Testing of Model Rotors (AATMR) Program and involved U.S. Government agencies and United Technologies Corporation (UTC). The four-bladed highly-instrumented rotor is a one-sixth (9.4 ft diameter) geometrically and aeroelastically scaled freely-articulated UTC model. The blade chord is 3.64 in and the blade tip has a 20° aft sweep from $r/R = 0.93$ to the tip. The test covered a broad range of conditions including low to mid-speed descent and level flight, as well as high speed forward flight. Extensive unsteady surface pressure measurements[36,19] were taken to match acoustic measurements[37] from nineteen microphones. The basic tunnel set-up is illustrated in Figure 21 which shows the model and the three microphones of present interest.

The CAMRAD.Mod1/HIRES codes are applied to one descent case: $\mu = 0.15$, $C_T/\sigma = 0.071$, $M_H = 0.64$, and $\alpha_s = 5.5°$. The windtunnel corrected mean rotor angle was 5.1°. No fuselage or test stand corrections

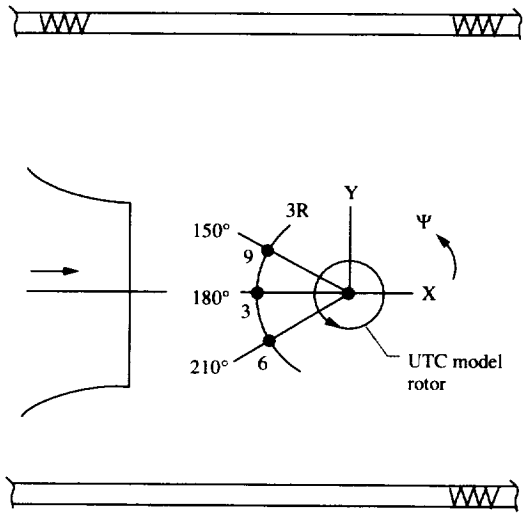

Figure 21: Plan view of the UTC model in the DNW open test section. The microphones of interest are shown. These are 25° down from the horizontal plan through the hub.

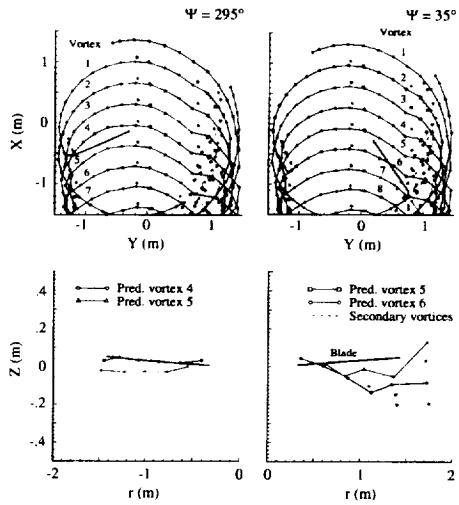

Figure 22: Predicted UTC model wake geometry for descent case. Format is similar to Figure 18(a).

were considered. This case was chosen as a typical strong BVI flight condition. For the predictions, the blade motions were computed by CAMRAD.Mod1 using the first 3 blade bending and torsion degrees of freedom, both include the control system as the first degree of freedom. The rotor was trimmed to the thrust and zero flapping by the use of the collective and cyclic pitch controls, as was done during the test. The multi-core roll-up model within CAMRAD.Mod1 was employed. The same definitions used for the HART model were used for the UTC model, including the same 9 core sizes and Equation 13 for r_v/R. HIRES and WOPWOP accounted for the straight and swept tip planform portions of the model. Figure 22 shows the calculated wake, presented in the same manner of Figure 18(a). The secondary vortices, evident on the advancing side are the result of combination of light negative and light positive loading (corresponding to both Figures 7 and 8) over most of the advancing side. The strength of the secondary vortex is generally stronger in this region than the that of the tip. However, it appears in the side view that the tip vortices can be closer to the blade during BVI.

Figure 23 is the presentation of the measured and predicted average acoustic-pressure time histories from the three microphones located in Figure 21. It is seen that while there is some over and under-prediction of the impulsive BVI noise,the overall levels and characteristics appear to be captured. It is noted that the present predictions match almost as well as the

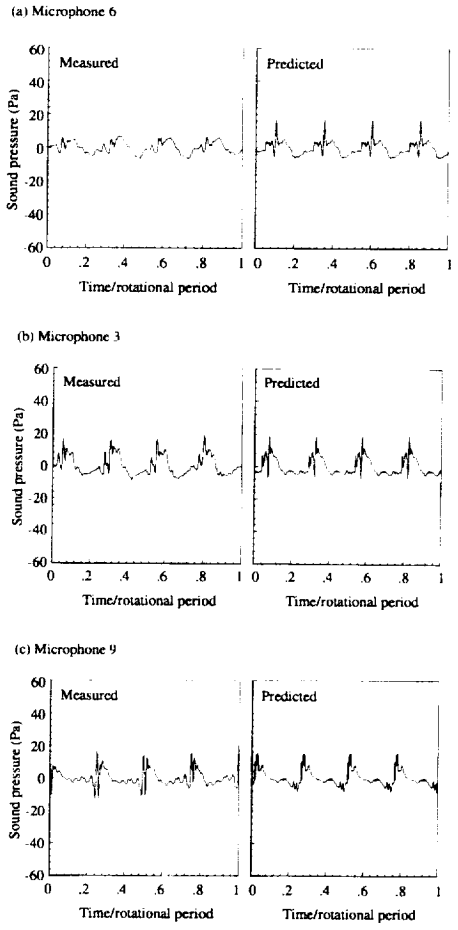

Figure 23: Measured and predicted UTC model acoustic pressure time history comparisons for three microphones.

corresponding case in Reference 37, where the actual measured surface pressures were used over a full-surface description in WOPWOP. However, it cannot be said at present how well the codes do for the full range of conditions that was considered in Reference 37. For this study, no other test conditions were examined.

JVX Tiltrotor Test

The proprotor of a tiltrotor vehicle configuration, with its high twist and large variation in blade chord and thickness, is a challenge, not only to the generality of the multi-core roll-up modeling, but also to the compact lifting-line aerodynamic and acoustic source representations in the present codes. A unique data base was obtained in the 1994 joint NASA/Army/Bell Helicopter Textron test of an isolated tiltrotor model at the NASA Langley Research Center. The test produced a comprehensive set of tiltrotor aerodynamic and acoustic data acquired for a range of forward flight conditions, typical of those flown for the full scale tiltrotor vehicle. Results of the acoustic measurements are presented by Marcolini, et al.[38]. A photograph of the isolated rotor model mounted in the 14- by 22-Foot Subsonic Tunnel test section is shown in Figure 24. The 3-bladed rotor model is a 15 percent scaled JVX tiltrotor, with a rotor diameter of 5.7 feet, a solidity of .114, a blade twist of -47.5° and a tip chord of 3.6 inches. The acoustic data acquired during the test were obtained on a horizontal plane $1.75R$ below the rotor using 2 traversing microphone arrays of 8 microphones each[38].

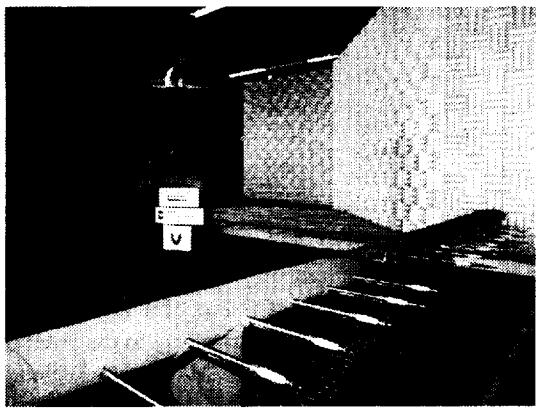

Figure 24: JVX tiltrotor model in the Langley 14 by 22 Foot Subsonic Tunnel

For prediction comparisons, one descent case is considered: μ=.17, C_T = 0.00984, and α_s = 3.15°. For the present predictions a corrected mean rotor angle of 5.05° is used. This differs from α_s by the sum of a −0.1° windtunnel wall effect and an estimated (and unvalidated) +2° test-installation upwash for the large test stand, microphone traverse, and flow curvature in the forward part of the test section (a thickened boundary layer is assumed with the acoustically treated floor in place). The multi-core roll-up vortex model were used in the same manner as for the HART and UTC helicopter models, including the multi-core definition and the r_v/R function, given in Equation (13). The blade motions were calculated by CAMRAD.Mod1 using 3 blade bending and 3 torsional degrees of freedom. The teetering rotor option with gimbal hub was used. The rotor was trimmed to the thrust and zero flapping by the use of the collective and cyclic pitch controls, as was done during the test. The Scully free-wake calculation was performed in the same manner with one exception. The free-wake tip core radius (used within the free-wake calculation only) was $.09R$ rather than the $.03R$ value that was used for the HART and UTC rotors. This relates to trim issues dealt with in the following section.

A plan view of the predicted wake geometry is shown in Figure 25. One blade, of the three bladed rotor, is shown at Ψ=70°. It is seen that secondary

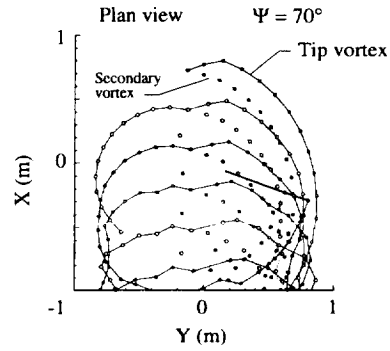

Figure 25: Predicted top view of wake geometry for the JVX.

vortices are present over most of the advancing side of the rotor. Figure 26 shows the measured and predicted mid-frequency BVI noise directivity. Each contour is divided due to the limited coverage of the two separate microphone arrays. The results are seen to be fair to good for direction and amplitude. The same level of agreement is found in the comparison between the measured and predicted acoustic pressure time histories shown in Figure 27.

More extensive comparisons and analyses for this proprotor test are given by Burley, et al.[39].

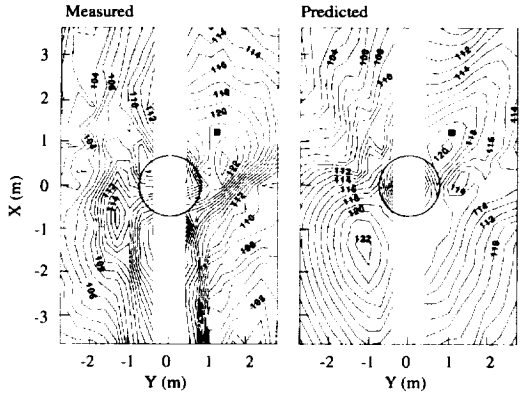

Figure 26: Measured and predicted BVI directivity level contour for the JVX. The symbol ■ indicates microphone location for acoustic pressure time histories in Figure 27.

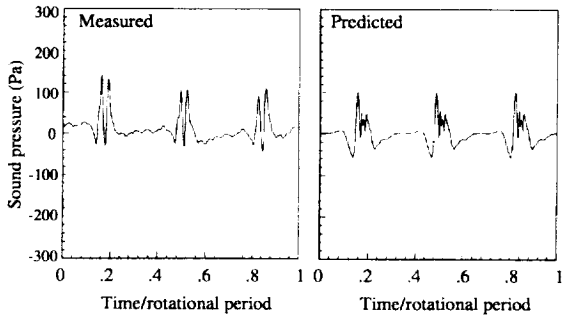

Figure 27: Measured and predicted acoustic pressure time histories for the JVX for microphone locations indicated in Figure 26.

Evaluation Of Results

Vortex Roll-up modeling - The effectiveness of the new multi-core roll-up modeling can be evaluated by comparing the present results to those obtained by simpler and more traditional vortex modeling. Figures 28, 29, and 30 show predictions corresponding to Figures 18, 19, and 20 for the HART BL(5.3°) and HHC-MV cases. These were obtained by not using the multi-core model and reverting back to an earlier method used. These predictions are similar but not identical to those in Reference 12, because a zero-moment trim was not then employed. The simpler method is to use a single 'no-roll-up' tip vortex, such as shown in Figure 2. In this case, the Γ assigned to the vortex at each azimuth is Γ_{+max}, obtained from the Γ distribution from the aerodynamic trim (see total bound circulation distribution of Figure 9). The vortex core r_c/R is set to 0.018 which is seen in Figure 15 to be roughly the

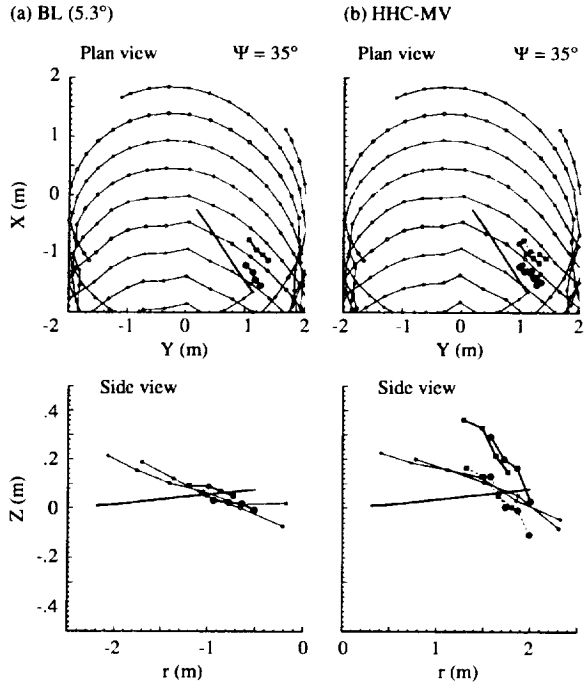

Figure 28: 'No-rollup' prediction of wake geometry corresponding to the HART BL(5.3°) and HHC-MV cases in Figure 18(a) and (b), respectively.

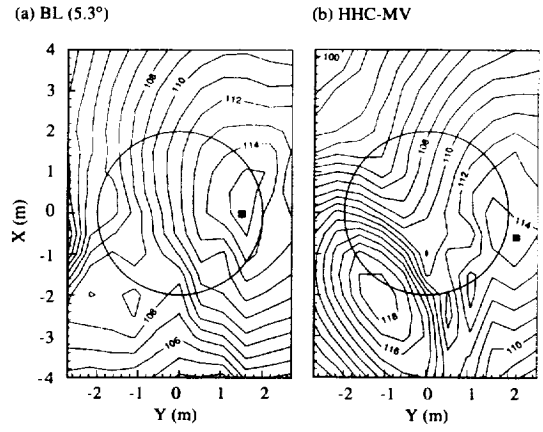

Figure 29: No-rollup' prediction of BVI noise directivity corresponding to the HART BL(5.3°) and HHC-MV case measurements in Figure 19(a) and (b), respectively.

average for the BL(5.3°) case. The vortex structure is defined by the 'Scully' vortex, Equation (1), or n =1 in Equation (3), which serves to reduce the maximum velocity amplitude, compared to our mult-core model use of n =2. This offsets the increase in vortex Γ values.

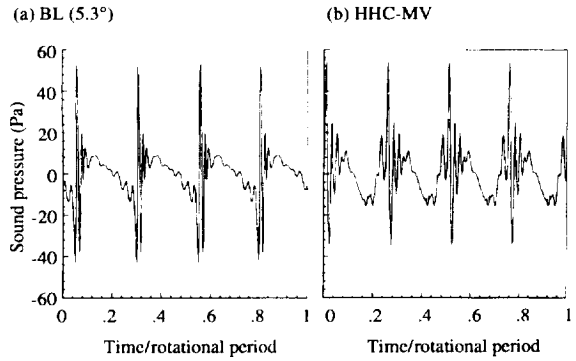

Figure 30: 'No-rollup' prediction of acoustic pressure time histories corresponding to the HART BL(5.3°) and HHC-MV case measurements in Figure 20(a) and (b), respectively.

The wake plot for the advancing side in Figure 28(a) for BL(5.3°) shows a lack of agreement in the top view positions of the vortex elements; compared to the roll-up calculation results of Figure 18(a). However, the vertical positions are equally well matched. For HHC-MV, in Figure 28(b), the no-roll-up case with its single vortex does not capture, of course, the dual vortex pairs seen in Figure 18(c). However, side view shows general agreement in the vertical and radial direction for the single vortices with the secondary vortex of the roll-up model. Noise directivity contours are shown in Figures 29(a) and (b), which correspond to Figures 19(a) and (c) for the roll-up calculations. It is seen that there is general agreement between the two calculation methods. This is also reflected in acoustic pressured time histories using the no-roll-up method compared to the roll-up method, i.e. compare Figures 30(a) and (b) to Figures 19(a) and (b), respectively.

It is important to point out that the results above do not so much indicate that the simpler approach is as adequate to predict the noise for the HART model, for these particular test conditions, as is it a validation of the multi-core roll-up modeling implementation. The wake comparisons show that the dominant BVI locations are well matched in the vertical and radial directions (the important 'miss distance') for both methods. For the HHC-MV case, the tip vortex of the vortex pair appears not to be an important BVI noise source, because it is above and off the tip near BVI. Therefore, here, the no-roll-up method noise predictions did not suffer from its lack of a secondary vortex. The reasonable noise level results using the no-roll-up model is the result of the chosen definition of the vortex structure, size, and strength, which evolved over a period of usage using BO-105 rotor model data. These can be regarded as tuning parameters, which would have to be reassessed with any change in model configuration. The present roll-up multi-core modeling was developed to help eliminate such choices. The following comparisons for the UTC and the JVX illustrate the significance and success of this modeling.

For the UTC rotor, Figure 31 shows the resulting wake pattern when the roll-up model is turned off. Comparing this with Figure 22, it is seen that the

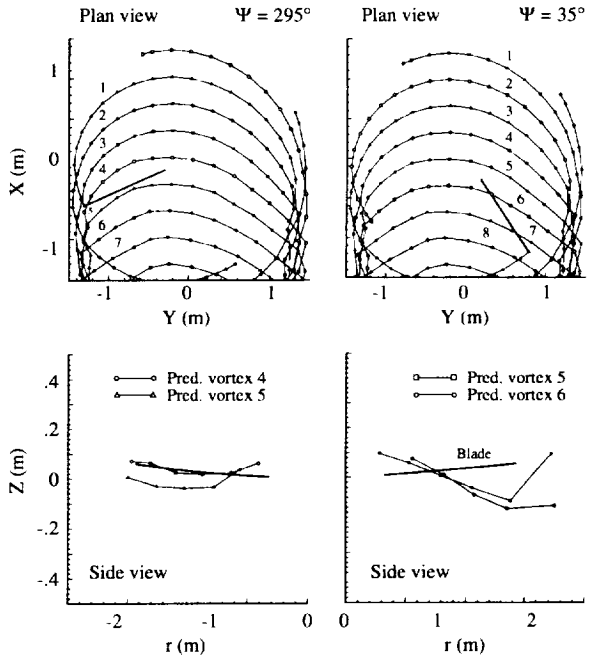

Figure 31: 'No-rollup' prediction of UTC model wake geometry corresponding to Figure 22.

no-roll-up tip vortex is basically matched with the roll-up model secondary vortex over the advancing side. Figure 32(a) and 32(b) show the no-roll-up predictions for the acoustic pressure time histories for microphones 6 and 3. The corresponding roll-up predictions are shown in Figures 23(a) and (b), respectively. Here, unlike the result for the HART rotor, the noise is not well predicted. The extreme amplitudes of the no-roll-up cases are the result of excessively strong tip vortices, whose strength is defined as Γ_{+max} from the total bound circulation distribution. Unlike the HART rotor (in its non-HHC cases), the UTC rotor is less loaded at the tip and, thus, the secondary vortex dominates due to heavier inboard loading. The multi-core modeling appears to properly account for this inboard bound circulation distribution and the effect of rotation of the blade in defining the vortex structure.

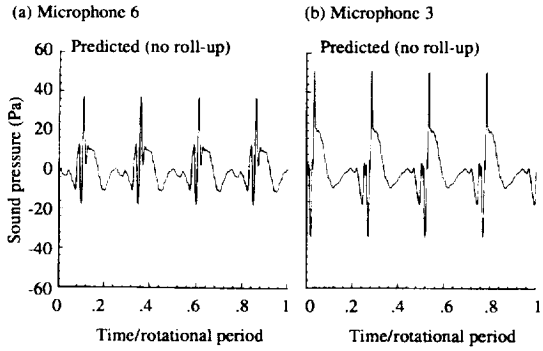

Figure 32: 'No-rollup' prediction of the UTC model acoustic pressure time histories microphones 6 and 9 corresponding to Figure 23.

The JVX proprotor model is, of course, even more loaded inboard than the UTC. Following the analogy of UTC results one would expect that the use of the no-roll-up method to even more over-predict the noise. The results for the no-roll-up method are shown in Figure 33(a) for the directivity and 33(b) for the acoustic pressure time history. Comparing these to Figures 26 and 27, respectively, it is seen that indeed the noise is increased over most of the directivity pattern and that the time history impulsive BVI noise is significantly over-predicted, when the multi-core roll-up model is not used.

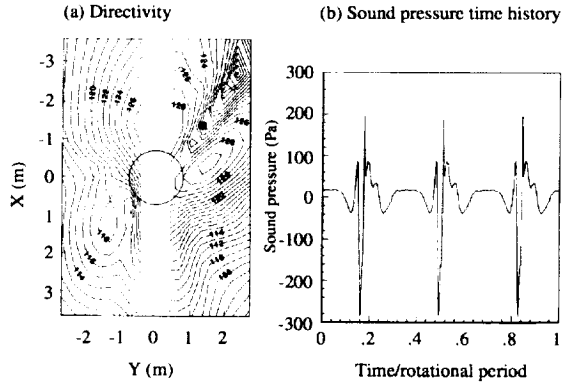

Figure 33: 'No-rollup' prediction of BVI noise for the JVX (a) directivity corresponding to Figure 26 and (b) acoustic pressure time history corresponding to Figure 27.

Issues of the Free-Wake Analysis - As mentioned previously, the use in CAMRAD.Mod1 of the Scully free-wake method[23] introduces limitations in our overall modeling of the wake. The present multi-core roll-up model anchors its vortices positions relative to this free-wake result. The Scully method has a very successful history, but is dated at present. The method is restricted to a single free-wake (freely distorting) tip vortex and one inboard vortex of prescribed motion. Although the multi-core (and multiple vortices) roll-up model is used in the aerodynamic trim and in HIRES and WOPWOP for the noise, this is lost in the free-wake calculations. The new free-wake models of Johnson[20] and Bagai and Leishman[26] with the ability to trail multiple free trailers offers promise in refining and generalizing the present multi-core roll-up approach. Until this is developed, however, the present results still indicate that CAMRAD.Mod1 can be successfully applied. This is true, of course, to the extent that basic features of the wake geometry are reasonably calculated.

The Scully free-wake calculations should be least accurate where the inboard of the blades are more heavily loaded than the tip region, which is true of the UTC and, particularly, for the JVX proprotor. However, the one UTC case calculated here using the free-wake in the 'standard' way did produce sensible comparisons. As described for the JVX, the 'standard' way was used but with an increased tip core radius (used only in the free-wake geometry calculation) in order to desensitize the observed tip vortices mutual influences and resultant geometry distortions. The $.09R$ value used is well within accepted values[40]. The geometry distortions resulted from unrealistically strong tip vortices, due to the Scully free-wake method's implicit assumption of heavy tip loading, whereas the proprotor is heavily loaded inboard. This follows an argument in the last section on the use of Γ_{+max} to define the tip vortex strengths, but here the issue is distorted wake geometry rather than the separate issue of BVI amplitudes. The use of $.09R$ core radius above to reduce distortions may not have been the optimum way to solve the distortion problem, because unrealistically strong vortices would still over-predict the induced downwash over the rotor disk. It may be possible that better methods could be developed to redefine the strengths of free-wake vortices by using the vortex segment stretching model, to account for high inboard loading. Some examination of such methods is dealt with in Reference 39.

Conclusions

The capabilities of CAMRAD.Mod1/HIRES to predict harmonic and impulsive BVI noise are summarized and then demonstrated for three different rotor configurations. Overall, the agreement to data quite good considering the significant differences between the rotor models. The HART (DLR) rotor is

four-bladed and hingeless with rectangular planform blades with light twist. The UTC rotor is four-bladed and freely-articulated with a constant chord planform blades with moderate to high twist and an aft sweep tip. The JVX proprotor (tiltrotor) is a three-bladed rotor assembly with a gimbaled hub and stiff high-twist blades, with large chord and thickness variations. The data from the HART program, using the German DLR BO-105 rotor model, was extensively employed and was the primary vehicle to validate the prediction method. The comparisons for the other two rotors demonstrated the generality of the developed models for significantly different rotor configurations.

The success of the noise prediction method was found to depend substantially on the new multi-core roll-up modeling of the rotor wake. This wake modeling was developed from classical wake roll-up concepts for fixed wings and applied to the rotor problem. Algorithms were developed to be compatible with the wake descriptions in CAMRAD. The codes were validated, with regard to vortex structure and swirl velocity, using the HART data. The method appears to be successful in determining the vortex structure and strength from the predicted aerodynamics, thus greatly reducing the need for tweaking vortex parameters. It is believed, however, that improvements in the free-wake analysis, as well as the addition of extra free-wake vortex trailers, in CAMRAD.Mod1 would further enhance the code's capability and dependability. In addition, overall enhancement of the predicabilty and physical understanding of rotor noise will depend on needed future testing and theoretical studies of the rotor wake development. There are a number of unresolved fundamental aerodynamic and aeroelastic issues.

CAMRAD.Mod1/HIRES appears to be sufficiently capable as a design tool. As an example, the calculations shown in this paper reveal the physics of the wake formation process and also, perhaps formally for the first time, the role that secondary vortices play in the impulsive BVI noise production. It is seen then that the commonly held concept, that just relieving the tip loading would weaken the tip vortex and thus reduce or eliminate BVI noise, does not hold. This may just cause the BVI producing vortex to be released from a more inboard position. Its strength, depends on the lift distribution, which is dependent on the rotor blade design. The current roll-up model implicitly accounts for the effect of blade design by utilizing lift distribution in defining the wake structure and strength. This has significant ramifications with regard to design methodology for noise reduction.

Acknowledgments

The authors would like to express sincere appreciation to the members of the HART test and prediction teams for their efforts before, during, and after the program that provided the excellent data base and physical insight. In particular, we would like to thank the Test Director, Wolf Splettstoesser of DLR for his exceptional leadership. Others from DLR, which we would like to thank, include: Wolfgang Geissler, Bernd Junker, Roland Kube, Ulrich Seelhorst, Klaus Schultz, Wolfgang Wagner, Berend van der Wall, and Hans-Jurgen Wirth. From ONERA, we would like to acknowledge Philippe Beaumier, Alain Boutier, Francis Micheli, and Pierre Spiegel. From DNW, the contributions of Edzard Mercker and Kurt Pengel are recognized. We also greatly appreciate our U.S. partners, the U.S. Army (AFDD) at NASA Ames, who developed and managed the HART program. Special thanks and gratitude go to Yung Yu, Chee Tung, and Judith Gallman.

We are also grateful to members of the JVX test program for providing the unique and high quality proprotor data. Acknowledged are Michael Marcolini, David Conner (AFDD), and Susan Gorton (AFDD) from NASA Langley; as well as John Brieger and Ben Settle of Bell Helicopter Textron. For the UTC data, we would like to thank the test teams from United Technologies Research Center, AFDD and NASA at the Ames and Langley Research Centers.

Appreciation is extended to Wayne Johnson of Johnson Aeronautics for a number of discussions which provided insight for CAMRAD and for rotorcraft, in general. Also, we would like to acknowledge useful dialogue with Thomas Beddoes of Westland Helicopters Ltd., U.K.

References

[1]Brooks, T. F., Booth, E. R., Jr., Splettstoesser, W. R., Schultz, K. J., Kube, R., Niesl, G., and Streby, O.: "Analysis of a Higher Harmonic Control Test to Reduce Blade Vortex Interaction Noise," *Journal of Aircraft*, Vol. 31, No. 6, Nov.-Dec. 1994, pp. 1341–1349.

[2]Prichard, D.S., Boyd, D.D., and Burley, C.L.: "NASA/Langley's CFD-Based BVI Rotor Noise Prediction System: (ROTONET/BVI) An Introduction and Users' Guide," *NASA TM* 109147, Nov. 1994.

[3]Brentner, K.S.: "Prediction of Helicopter Rotor Discrete Frequency Noise," *NASA TM* 87721, Oct. 1986.

[4]Farassat, F.: "Theory Of Noise Generation From Moving Bodies With An Application To Helicopter Rotors," *NASA TR* R-451, 1975.

[5]Farassat, F., and Myers, M.K.: "Extension of Kirchhoff's Formula To Radiation from Moving Surfaces," *Journal of Sound And Vibration*, Vol. 123. No. 3, 1988, pp. 451–461.

[6]Farassat, F.: "Quadrupole Source in Prediction of Noise of Rotating Blades—A New Source Description," AIAA Paper 87-2675, 1987.

[7]Brentner, K.S.: "An Efficient and Robust Method for Prediction Helicopter Rotor High-Speed Impulsive Noise," AIAA Paper 96-0151, Jan. 1996.

[8]Splettstoesser, W.R., Kube, R., Seelhorst, U., Wagner, W., Boutier, A., Micheli, F., Mercker, E., and Pengel, K.: "Key Results from a Higher Harmonic Control Aeroacoustic Rotor Test (HART) in the German-Dutch Wind Tunnel," 21th European Rotorcraft Forum, Saint-Petersburg, Russia, Aug./Sept. 1995.

[9]Yu, Y.H., Gmelin, B.L., Heller, H.H., Philipe, J.J., Mercker, E., Preisser, J.S.: "HHC Aeroacoustic Rotor Test at the DNW—The Joint German/French/US Project," 20th European Rotorcraft Forum, Amsterdam, The Netherlands, Sept. 1994.

[10]Gmelin, B.L., Heller, H.H., Mercker, E., Philippe, J.J., Preisser, J.S, and Yu, Y.H.: "The HART Programme, a Quadrilateral Cooperative Research Effort," AHS 51st Annual Forum, Ft. Worth, TX, May 1995.

[11]Beaumier, P., Prieur, J., Rahier, G., Spiegel, P., Demargne, A., Tung, C., Gallman, J., Yu, Y. H., Kube, R., Van der Wall, B. G., Schultz, K., Splettstoesser, W., Brooks, T. F., Burley, C. L., and Boyd, D. D.: "Effect of Higher Harmonic Control on Helicopter Rotor Blade-Vortex Interaction Noise: Prediction and Initial Validation," AGARD Symposium on Aerodynamics & Aeroacoustic of Rotorcraft, Berlin, Germany, Oct. 1994.

[12]Tung, C., Gallman, J., Kube, R., Wagner, W., Van der Wall, B., Brooks, T., Burley, C., Boyd, D., Rahier, G., and Beaumier, P.: "Prediction and Measurement of Blade-Vortex Interaction Loading," 1st Joint CEAS/AIAA Aeroacoustics Conference, Munich, Germany, June 1995.

[13]Gallman, J., Tung, C., Schultz, K., Splettstoesser, W., Buchholz, H., Spiegel, P., Burley, C., Brooks, T., and Boyd, D.: "Effect of Wake Structure on Blade-Vortex Interaction Phenomena: Acoustic Prediction and Validation," 1st Joint CEAS/AIAA Aeroacoustics Conference, Munich, Germany, June 1995.

[14]Beaumier, P. and Spiegel, P.: "Validation of ONERA Aeroacoustic Prediction Methods for Blade-Vortex Interaction Using HART Tests Results. AHS 51th Annual Forum of the American Helicopter Society, Fort Worth, TX, May 1995.

[15]Johnson, W.: "A Comprehensive Analytical Model of Rotorcraft Aerodynamics and Dynamics, Part 1-Analysis and Development," NASA TM-81182, June 1980.

16Beddoes, T.S.: "Two and Three Dimensional Indicial Methods for Rotor Dynamic Airloads," AHS National Specialists Meeting on Rotorcraft Dynamics, Arlington, TX, Nov. 1989.

[17]Beddoes, T.S.: "A Near Wake Dynamic Model," AHS Specialists Meeting on Aerodynamics and Aeroacoustics, Arlington, TX, Feb. 1987.

[18]Ffowcs Williams, J.E. and Hawkings, D.L.: "Sound Generation by Turbulence and Surfaces in Arbitrary Motion," *Philosophical Transactions of the Royal Society of London, Series A*, Vol. 264, May 1969, pp. 321–342.

[19]Lorber, P.F.: "Blade-Vortex Interaction Data Obtained from a Pressure-Instrumented Model Rotor at the DNW," AHS/RAS International Technical Specialists Meeting on Rotorcraft Acoustics and Rotor Fluid Dynamics, Philadelphia PA, October 1991.

[20]Johnson, W.: "A General Free Wake Geometry Calculation for Wings and Rotors," AHS 51st Annual Forum, Fort Worth, TX, May 1995.

[21]Johnson, W.: "Airloads and Wake Models for a Comprehensive Helicopter Analysis," *Vertica*, Vol. 14, No. 3, 1990.

[22]Scully, M.P.: "Computation of Helicopter Rotor Wake Geometry and Its Influence on Rotor Harmonic Airloads," Massachusetts Institute of Technology, ASRL TR 178-1, March 1975.

[23]Johnson, W.: Helicopter Theory, Princeton Univ. Press, 1980, p. 539.

[24]Betz, A.: "Verhalten von Wirbelsystemen," *Z.f.a.M.M.*, Vol. 12, No. 3, June 1932, 164–174; see also translation: "Behavior of Vortex Systems," NACA TM 713, June 1933.

[25]Vatistas, G.H., Kozel, V., and Mih, W.C.: "A Simpler Model for Concentrated Vortices," *Experiments in Fluids*, Vol. 11, 1991, pp. 73–76.

[26]Bagai, A. and Leishman, J.G.: "Rotor Free-Wake Modeling Using a Pseudo-Implicit Technique—Including Comparisons with Experimental Data," *Journal of the American Helicopter Society*, Vol. 40, (3), July 1995, pp.29–41.

[27]Donaldson, C. duP., and Bilanin, A. J.: "Vortex Wakes of Conventional Aircraft," AGARDograph No. 204, May 1975.

[28]Bliss, D. B.: "Prediction of Tip Vortex Self-Induced Motion Parameters in Terms of Rotor Blade Loading," AHS National Specialist's Meeting on Aerodynamics and Aeroacoustics, Arlington, TX, Feb. 1987.

[29]Jumper, S.J.: "Computer Prediction of Three Dimensional Potential Flow Fields in Which Aircraft Propellers Operate (Computer Program Description and Users Manual)," PSU-AERO-R-79/80-25, Penn State University, Aug. 1979.

[30]Brooks, T.F., and Burley, C.L.: "A Wind Tunnel Wall Correction Model for Helicopters in Open, Closed, and Partially Open Rectangular Test Sections," NASA TM (to be published) Aug. 1996.

[31]Langer, H.J., Peterson, R.L., and Maier, T.: "An Experimental Evaluation of Wind Tunnel Wall Correction Methods for Helicopter Performance," AHS 46th Annual Forum, Washington DC, June 1996.

[32]Seelhorst, U., Butefisch, K.A., and Sauerland, K.H.: "Three Component Laser-Doppler-Velocimeter Development for Large Wind Tunnel," ICIASF 1993 Record, pp.33.1–33.7, 1993.

[33]Boutier, A., Lefevre, J., Soulevant, D., Dunand, F.: "2D Laser Velocimetry Near Helicopter Blades in DNW (NLR)," ICIASF 1993 Record, 1993, pp. 32.1–32.8.

[34]Mercker, E., Pengel, K.: "Flow Visualization of Helicopter Blade Tip Vortices - A Qualitative Technique to Determine the Trajectory and the Position of the Tip Vortex Pattern of a Model Rotor," 18th European Rotorcraft Forum, Avignon, France 1992.

[35]Yu, Y.H., Liu, S.R., Landgrebe, A.J., Lorber, P.F., Jordan, D.E., Pallack, M.J., and Martin, R.M.: "Aerodynamic and Acoustic Test of a United Technologies' Model Scale Rotor at DNW," AHS 46th Annual Forum, Washington DC, May 1990.

[36]Liu, S.R. and Marcolini, M.A.: "The Acoustic Results of a United Technologies Scale Model Helicopter Rotor Tested at DNW," AHS 46th Annual Forum, Washington DC, May 1990.

[37]Visintainer, J.A., Burley, C.L., Marcolini, M.A., and Liu, R.L.: "Acoustic Predictions Using Pressures from a Model Rotor in the DNW," AHS 47th Annual Forum, Phoenix, AZ, May 1991.

[38]Marcolini, M.A., Conner, D.A., Brieger, J.T., Becker, L.E., and Smith, C.D.: "Noise Characteristics of a Model Tiltrotor," AHS 51st Annual Forum, Fort Worth, TX, May, 1995.

[39]Burley, C.L., Marcolini, M.A., Brand, A.G., and Conner, D.A.: "Tiltrotor Aeroacoustic Code (TRAC) Predictions and Comparisons with Measurement," AHS 52nd Annual Forum, Washington D.C., June 1996.

[40]Johnson, W.: "Calculation of Blade-Vortex Interaction Airloads on Helicopter Rotors," *Journal of Aircraft*, Vol. 26, No. 5, 1989.